SATELLITE-BASED LAVA FLOW MORPHOLOGY CLASSIFICATION AT MOUNT KĪLAUEA, HAWAI'I

CLAUDIA SAURO

Thesis submitted to the University of Ottawa

in partial Fulfillment of the requirements for the

degree of M.Sc. of Geography

Department of Geography, Environment and Geomatics

Faculty of Arts

University of Ottawa

Keywords: Remote Sensing, Lava Flow Morphology, Object-Based Classification

Abstract

Accurately mapping lava flow morphologies is important for understanding volcanic processes evaluating hazards, and for supporting fieldwork planning. However, differentiating between the two most common basaltic morphologies, pāhoehoe and ‘a’ā, in remote sensing data has been challenging due to their similar mineralogical compositions and spectral overlap. This study evaluates an object-based classification methodology using the freely available Sentinel-1 C-band Synthetic Aperture Radar (SAR) and Sentinel-2 optical imagery to classify the lava flow morphologies on the 2018 lower East Rift Zone (ERZ) eruption of Mount Kīlauea, Hawai’i. Six Segment Mean Shift (SMS) parameter sets and sixteen three-band composites were tested under two validation methods: Definition-based (Pāhoehoe vs. ‘A’ā) and Textural-based (Smooth vs. Rough). Classification was done using SMS segmentation followed by K-Means clustering, with results compared to validation datasets created from high-resolution drone imagery. The highest overall accuracies (OA) were 86.31% (Definition-based) using a multi-sensor (Sentinel-1 and Sentinel-2) composite, and 88.69% (Textural-based) using Sentinel-2 RGB bands. Grey-Level Co-occurrence Matrix (GLCM) texture features (contrast, homogeneity, energy, entropy) showed consistent differences between the morphologies, supporting their potential for semi- or fully unsupervised classification, though the analysis here remained exploratory. Terrain analysis showed that Sentinel-2 was more susceptible to misclassifications related to the slope aspects Northness and Eastness, while terrain effects were negligible for Sentinel-1. The overall findings show that freely available multi-sensor data, combined with object-based segmentation and texture analysis, can reliably map lava flow morphologies, highlighting ways for improving automated classification workflows for volcanic morphological mapping.

Acknowledgments

I would like to express my sincere gratitude to my supervisor, Dr. Anders Knudby, for his understanding, patience, and guidance throughout this research. Your support and mentorship during times when the scope of my work felt overwhelming was invaluable to the completion of my thesis. I am also grateful to my committee members, Dr. Koreen Millard and Dr. Luke Copland, whose constructive feedback and insights greatly strengthened my work. I am also eternally grateful for having had the opportunity to conduct fieldwork in Hawai'i in order to collect my validation data. My time spent on the Big Island was not only an experience that advanced my research, but it also made my childhood dream of studying volcanoes a reality.

I would also like to extend my thanks to my colleagues at Environment and Climate Change Canada for their encouragement and wisdom throughout this process, with special mention to Cary, Joseph, Carlos, Olivier, and Kevin. You, along with the rest of the team, have always rooted for my success and kept me grounded. Finally, I am deeply grateful to my family and friends for their unwavering support and reassurance, who reminded me every day that I could see this project through to the end.

Table of Contents

List of Figures

List of Tables

List of Equations

Chapter 1. Introduction

Volcanic hazards can have catastrophic local and global impacts, making the monitoring of volcanic processes essential to risk assessment and disaster management planning (Rösch & Plank, 2022). Understanding the history of a volcano is critical for the evaluation of future volcanic hazards and risks (Lockwood et al., 2022). However, of the approximately 1500 active subaerial volcanoes across the globe, less than 10% are regularly monitored from the ground (Cigna et al., 2020). Obtaining data in the field can be not only expensive due to transportation, equipment, and training costs, but also complicated and dangerous, especially in areas of high eruption frequency. In this context, remote sensing technologies are a useful tool in the study of volcanic activity around the world.

Using remote sensing can save on time and cost, reduce or eliminate risk, and allow for access to data worldwide. Safety is especially important with regard to the monitoring of live volcanic eruptions or for use in lava flow classification at high-eruption-frequency volcanoes. The classification of lava flows is an important step in understanding the eruptive nature of volcanoes and volcanic fields (Al Shehri & Gudmundsson, 2019). Understanding the activity of a volcano also provides valuable information in areas with human settlement and activity (Li et al., 2017-a). This type of information is important for post-eruption environmental impact assessments, land planning, and the settlement of populations around volcanically active regions (Li et al., 2017-a). The use of remote sensing is growing among volcanologists, demonstrated by the benefits of these technologies through the increase in knowledge about volcanoes that pose risks to local communities, critical infrastructure, and business (Cigna et al., 2020).

Lava flows are influenced by the mineralogical compositions and temperatures of the magma at volcanic locations, of which there are three basic types: basaltic, andesitic, and rhyolitic (Lockwood et al., 2022, p. 76). Basaltic magma has an eruptive temperature of ~1,200 °C (measured at the vent during the eruption) and is associated with non-explosive eruptions due to its lower silica (SiO_2) content (45-52%). In contrast, rhyolitic magma erupts at temperatures of ~800 °C and 73-77% SiO_2, which produces the most explosive eruptions. Andesitic magma has intermediate temperatures and SiO_2 content, meaning it produces intermediate eruptions (Philpotts & Ague, 2009, p. 23). Basaltic magma is the most commonly found magma on Earth (Lockwood et al., 2022, p. 74) and will be the focus of this study. The most common basaltic lava flows, pāhoehoe and 'a'ā, have similar mineralogical compositions but act very differently as they flow: pāhoehoe lava moves and cools slowly, while a'ā moves and cools quickly, a difference that results in remarkably different morphologies. Although both are basaltic in nature, their viscosities are determined largely by the initial eruptive temperature (with subsequent cooling), in addition to factors related to eruption dynamics and topography (Lockwood et al., 2022, p. 127).

Many studies on the topic of lava flow classification have been published within the last decade as satellite technologies continue to improve, providing enhanced spatial, temporal, and spectral resolutions (e.g., Aldeghi et al., 2019; Amici et al., 2014, Carr et al., 2021, Ghuffar, 2018). The classification of lava flows using remote sensing in high-eruption-frequency areas is complicated for two main reasons: the spatial overlapping of lava flows of different ages, and the fact that they exhibit similar spectral signatures because of their comparable mineralogical composition and morphology when emplaced within a short period of time (Aufaristama et al., 2019; Corradino et al., 2019).

In this study, I developed and evaluated a methodology to classify lava flow morphologies, specifically ‘a‘ā and pāhoehoe, using freely available remote sensing imagery. This study focused on the 2018 eruption of Mount Kīlauea’s lower East Rift Zone found on the Island of Hawai’i (also known as the Big Island). This volcano is well-documented and actively studied and monitored by the United States Geological Survey (USGS). Mount Kīlauea is considered to be the world’s most active volcano (Sheth, 2003). Due to its high eruption frequency and the presence of both basaltic lava flow morphologies, this site was ideal for evaluating surface texture classification approaches.

The primary objective of this study was to assess the feasibility of using freely available remote sensing data for lava flow classification, with the broader goal of advancing the mapping and interpretation of complex volcanic surfaces. This was done by implementing an object-based, segmentation workflow using the Segment Mean Shift (SMS) algorithm, testing six different parameters sets and sixteen band combinations derived from Sentinel-2 optical, and Sentinel-1 SAR imagery. These combinations were systematically tested to determine optimal configurations for segmenting the lava flow’s surface textures, while evaluating single-sensor and multi-sensor combinations. These configurations were evaluated using two validation strategies to determine the effect of transitional lava flow morphologies on the classification: one based on common definitions of ‘a‘ā and pāhoehoe, where transitional rubbly pāhoehoe was grouped with pāhoehoe, and the other based on visual surface texture, where rubbly pāhoehoe was grouped with ‘a‘ā in a smooth versus rough classification.

The secondary objective of this study was to determine whether Grey-Level Co-occurrence Matrix (GLCM) texture metrics, calculated from the segmented band combinations, could reliably characterize the lava’s surface roughness and support future efforts to automate the class labeling process, making the workflow less supervised. The findings have implications for improving the consistency and scalability of lava flow classification, particularly in remote volcanic regions.

Finally, the effects of terrain on the classification results were evaluated to better understand how the volcanic landscape may or may not influence classification performance.

Chapter 2. Literature Review

2.1 Historical View of Remote Sensing of Volcanoes

Satellite imagery has been used to study and monitor volcanoes from afar since the 1960s, when the first published use of thermal imagery, captured by the Nimbus I High-Resolution Infrared Radiometer, was released by Gawarecki et al. (1965) to compare the thermal radiance of Mount Kīlauea and its neighbour Mauna Loa (Pyle et al., 2013). Following the 1965 publication, thermal imaging remained the focus of studies of active volcanoes for several decades (Pyle et al., 2013), and it was not until the late 1980s that thermal imaging was used for more than just the study of active volcanoes. Multispectral thermal infrared imaging was used to map cooled lava flows, demonstrating its potential as a tool for geologic mapping of young volcanic terrains (Kahle et al., 1988). Classifying lava flows became more frequent as satellite technologies with higher spatial and spectral resolution became available and many newer studies tackled the classification issue. For example, the role of remote sensing in volcano monitoring expanded to include new sensing technologies such as thermal imaging and radar interferometry, and new data applications such as hazard assessments (Oppenheimer, 1997; Francis & Rothery, 2000). This was followed by studies demonstrating how multi-sensor approaches, integrating radar and multispectral data, could be used to analyze lava flow characteristics (Rowland et al., 2003).

In the last 15 years, there has been global use of both multispectral and hyperspectral imagery in the classification of lava flows, at locations such as Mount Etna, Italy (Amici et al., 2013), Mount Teide in the Canary Islands (Amici et al., 2014), and the Holuhraun lava field in Iceland (Aufaristama et al., 2019). In more recent years, machine learning has also been adopted to extract information from imagery at locations such as Mount Etna (Corradino et al., 2019), at Fogo Island (Corradino et al., 2021), and at Nyamuragira volcano in the Democratic Republic of the Congo (Li et al., 2017-b). Optical imagery has been proven to efficiently map lava flow extents, particularly for delineating active flows (Corradino et al., 2019; Musacchio et al., 2024), as well as for distinguishing and dating overlapping lava flows of different ages (Abrams et al., 1991; Li et al., 2017-a). The study of volcanic activity has grown alongside the emergence of more advanced satellite imaging and classification technologies, and it continues to evolve as new methods of collecting, monitoring, and analyzing data develop.

Radar imagery has proven to be useful in mapping and tracking lava flows when used with other forms of imagery, such as thermal and/or optical imagery. Radar data combined with optical imagery can be used to calculate lava flow area and thickness to produce lava flow maps (Lu et al., 2004), as well as to improve the accuracy and reliability of lava flow mapping during active eruptions (Corradino et al., 2021). Radar played an important role in mapping the virtually unobserved 1997 eruption of Okmok Volcano, found in a remote area of the eastern Aleutian Islands, where radar imagery from ERS-1 and ERS-2, RADARSAT and Japanese Earth Resources Satellite (JERS) sensors were used to evaluate post-eruption conditions, while AirSAR data was used to create a digital elevation model (DEM) for pre-eruption conditions (Patrick et al., 2003). Radar has also been used at Mount Kīlauea to calculate the statistical properties of surface roughness, with an additional focus on radar backscatter providing insights into the nature of lava flow texture and its impact on radar response at various incidence angles and wavelengths (Campbell & Shepard, 1996). As such, radar imagery has emerged as a valuable tool, demonstrating utility both in integration with other types of imagery, and as an independent data source. By harnessing the unique capabilities of radar imagery, researchers have expanded their understanding of volcanic dynamics and improved their ability to monitor and analyze volcanic processes.

2.2 Types of Lava Flow Morphologies

Subaerial lava flows are commonly categorized based on their morphology once cooled, falling into three primary roughness-based classes (Figure 1). The two most prevalent forms of cooled lava flows are referred to as pāhoehoe or 'a'ā, named after whether these were easy to traverse on foot, or not, by Native Hawaiian communities of the past. These terms were introduced into the scientific literature in 1884 by C.E. Dutton (Lockwood et al., 2022, p. 127). Pāhoehoe appears as a smooth, hummocky surface that would be easily traversed by foot (Lockwood et al., 2022, p. 119) and is less viscous while actively flowing (Peterson & Tilling, 1980). In contrast, 'a'ā is covered with loose, rough, spiny rubble, making it more difficult to traverse (Lockwood et al., 2022, p. 119) due to the more jagged texture (Mazzarini et al., 2007), as well as generally having higher viscosity values (Figure 2; Di Fiore et al., 2021; Peterson & Tilling, 1980). Most Hawaiian lavas are extruded as pāhoehoe and transition to 'a'ā when certain flow conditions are met (Peterson & Tilling, 1980; section 2.3). Today, the common definitions for these are: pāhoehoe, "Smooth, undulating, or corded volcanic lava" (Oxford University Press, n.d.-a); 'a'ā, "a rough, jagged surface covered with loose clinkers" (Oxford University Press, n.d.-b).

Other classes of lava flow morphologies are blocky lava, sometimes further differentiated as "blocky-lithic" and "blocky-glassy" (Lockwood et al., 2022, p. 119), sometimes (but not always) considered to be a subcategory of 'a'ā (Lockwood et al., 2022, p. 159; MacDonald, 1972). These types of lava flow are quite thick, move slowly, have large angular blocks that are generally smoother than the smaller 'a'ā blocks, and are more commonly associated with andesitic lava flows emanating from domes (Kilburn, 2000; Lockwood et al., 2022, p. 159).

Pāhoehoe flows, the most common and abundant of the flows discussed (Peckyno, 2010), can also be separated into subcategories based on their surface textures. For example, ropy pāhoehoe is described as areas where the crust wrinkles and folds in such a way that it resembles coils of rope; this turns into entrail pāhoehoe when steep slopes make the ropy texture resemble a "great heap of intestines" of overlapping pāhoehoe toes (Lockwood et al., 2022, p. 143). Field observations and remotely sensed imagery at a Mauna Ulu site in Hawai'i have been used to classify pāhoehoe lava into distinct surface units based on differences in colour, texture, and morphology (Byrnes et al., 2004). This demonstrates that although some lava flows in a study site may be of the same class, differences in textural features between subclasses can allow them to be further differentiated.

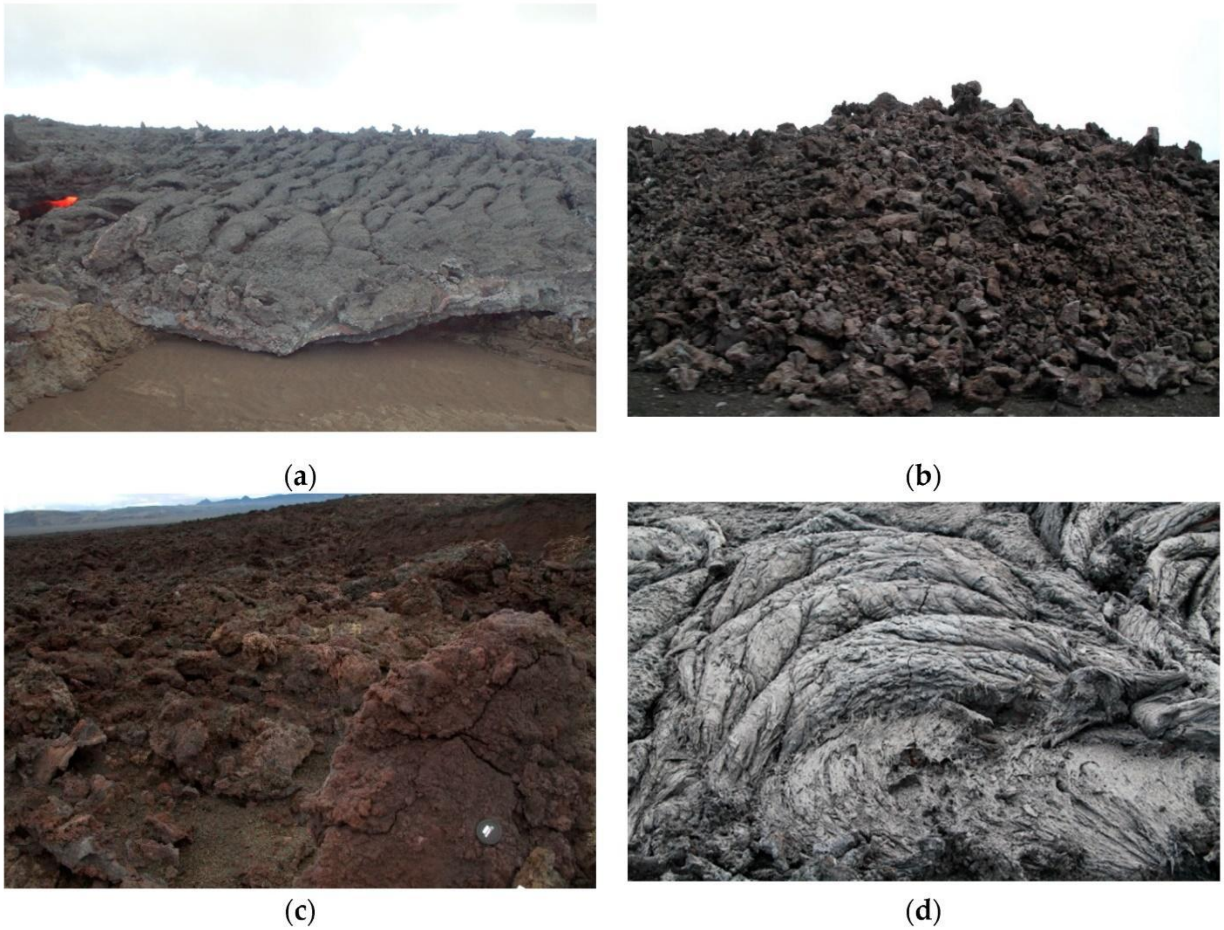

Figure 1. Figure adapted from Aufaristama et al., 2020. Surficial morphologies of lava flows found at the 2014–2015 lava flow at Holuhraun in Iceland. (a) Spiny pāhoehoe, (b) rubbly 'a'ā, (c) blocky lava, and (d) ropy pāhoehoe. Photos were taken by Thorvaldur Thordarson (a), G.B.M. Pedersen (b) and (d), and Muhammad Aufaristama (c).

The diversity of lava flow morphologies is linked to their distinct surface roughness characteristics at varying scales. The descriptive Surface Roughness Scale was created based on field measurements of crustal material on lava flow surfaces and qualitative notes taken in the field describing the appearance of lava flows at a wide range of scales (Tolometti et al., 2020). This can be used as a general guide to visually differentiate pāhoehoe, 'a'ā, and blocky lava flows. From these descriptions and measurements, it was found that 'a'ā lava flows exhibit a rough and jagged surface with conchoidal fractures, appearing roughest at the meter-to-decimeter scale. In contrast, various forms of pāhoehoe lava flow, such as smooth, hummocky, rubbly, and slabby, show differing roughness patterns at scales ranging from kilometers to centimeters; consequently, rubbly pāhoehoe and 'a'ā flows can have similar roughness at the dm-scale, making them more difficult to differentiate (Tolometti et al., 2020). Rubbly pāhoehoe appears blockier due to mechanical fragmentation, while ‘a‘ā clinker is the result of turbulent flow. Rubbly pāhoehoe is a transitional lava flow morphology that retains the internal structure of pāhoehoe but develops a fragmented, broken surface due to brittle crust disruption (Guilbaud et al., 2005), while ‘a‘ā clinker consists of jagged, spinose lava fragments formed by viscous tearing as the lava advances (Neish et al., 2016).

2.3 Transition from Pāhoehoe to 'A'ā

The transition from pāhoehoe to 'a'ā occurs when critical changes in lava flow conditions disrupts its initially smooth behaviour. Pāhoehoe typically forms when lava slows and cools due to increasing viscosity over time and distance from the vent (Peterson & Tilling, 1980). However, if flow conditions force the lava to continue moving despite this cooling, internal shear and turbulence can increase beyond a critical threshold, resulting in a morphological change to ‘a‘ā (Peterson & Tilling, 1980; Figure 2). This transition tends to occur when lava is subjected to mechanical disturbances such as vigorous fountaining, steep terrain, or plunging over ledges, all of which can increase internal deformation and flow instability (MacDonald, 1953). These disruptions break the crust of a pāhoehoe flow, transforming it into the rough texture characteristic of ‘a‘ā. Multiple factors can trigger this change, including changes in slope, prolonged degassing, or heat loss, which leads to pāhoehoe flows irreversibly transitioning to 'a'ā (Hawaiian Volcano Observatory, 1999; Peterson & Tilling, 1980). Because such conditions vary between eruptions and flow paths, the exact threshold at which pāhoehoe transforms into ‘a‘ā is not fixed (Figure 2 (b); Di Fiore et al., 2021).

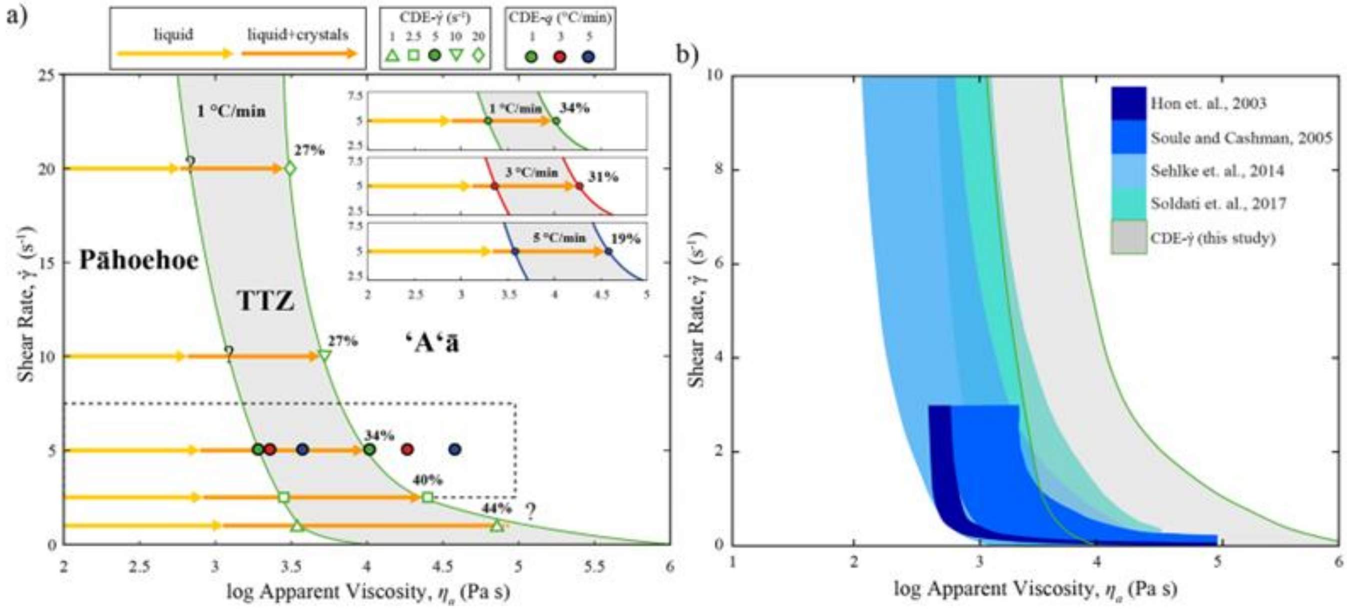

Figure 2. Shear rate versus the logarithm of the apparent viscosity diagram for lava flows, adapted from Di Fiore et al. (2021). (a) The shaded area represents the "transition threshold zone" (TTZ) separating pāhoehoe and 'a'ā flow regimes. Green-filled and empty symbols represent CDE-$\dot{\gamma}$ data used to define TTZ boundaries. The inset shows TTZ modification due to different cooling rates (CDE-q data as filled circles). Crystal-free melt and melt + crystals viscosity paths (yellow and orange lines) depict constant shear rate behavior. Numbers at the line ends indicate the estimated crystal fraction at viscous rupture. The lower TTZ limit is inferred from data (question marks). (b) displays TTZ fields from this study and literature data, delineating pāhoehoe and 'a'ā morphologies, including experiments and observations on basalts (Soule & Cashman, 2005; Sehlke et al., 2014; Soldati et al., 2017; Hon et al., 2003).

In Hawai'i, lava flow rates exceeding 5-10 m^3/s are generally associated with the formation of 'a'ā rather than pāhoehoe (Francis & Oppenheimer, 2003). While this measure (m^3/s) represents volumetric discharge rate, it serves as a proxy for how rapidly lava is moving downslope. This rate can inversely relate to lava viscosity, where higher flow rates often correspond to lower viscosities. However, this relationship is not absolute, as shear strain and cooling rate are also dynamic and play a role in determining surface morphology (Chevrel et al., 2019). Experimental studies in Hawai'i have further shown that the transition from pāhoehoe to 'a'ā typically occurs at temperatures between 1170-1200 °C, with dynamic viscosities ranging from 100-1000 Pa·s depending on strain rate applied (Sehlke et al., 2014; Figure 2b).

2.4 Limitations of Lava Flow Classification

There have been numerous studies using remote sensing to map lava flows, but they often use different criteria and sensors and vary in the level of detail and the definition and number of classes used. As such, the methods behind lava flow classification have yet to be standardized. Nonetheless, most studies on this topic agree on the fact that lava flows can be differentiated on the basis of their surficial morphology and spectral differences.

Spaceborne sensors are the most widely used data source for lava flow classification (Crown & Ramsey, 2017), but they have limitations, particularly with regards to mapping lava flows of different ages. While pāhoehoe and 'a'ā can generally be differentiated due to their morphological differences, it becomes more challenging to differentiate between the same types of lava flows, such as two overlapping pāhoehoe flows from separate eruptions, due to their similar spectral and mineralogical composition (Abrams et al., 1991; Aufaristama et al., 2019; Corradino et al., 2019). Differences in single-pixel point spectra among four pāhoehoe sites have been observed in visible and near-infrared (VNIR) and thermal infrared bands, revealing spectral variability in lava flows (Byrnes et al., 2004). Although spectral similarity is a limiting factor in certain cases, spectral reflectance remains a valuable property for monitoring and classifying lava flows (Al Shehri & Gudmundsson, 2019) as variations in texture, grain size, and the degree of weathering can still produce distinguishable spectral signatures, even among flows of the same type (Aufaristama et al., 2019).

Another key limitation of remote sensing-based lava flow classification is the presence of mixed pixels, where the recorded spectrum represents a weighted average of multiple surface types within a single pixel. This is a problem particularly pronounced when mapping heterogenous lava surfaces and is strongly influenced by sensor resolution and patch size (Aufaristama et al., 2019;

Byrnes et al., 2004). Linear spectral mixture analysis (LSMA) can be used to address the mixed-pixel problem by modeling pixel spectra through a combination of endmembers weighted by their respective abundances, contributing to the total reflectance of the mixed pixel (Aufaristama et al., 2019). However, this issue is mainly of concern in areas where lava flows are small relative to the pixel size of the sensor used, or where lava flows are overlapping and their edges fall within the same pixels as other flows. Mixed pixels are a negligible issue if the pixel size is sufficiently small for the lava flows being studied.

Limitations related to spectral similarity and mixed pixels can both be partially overcome by utilizing remote sensing data with higher spatial and spectral resolutions, by applying better-performing classifiers or by changing the way the classification is done, from pixel-based to object-based approaches (Li et al., 2017-b). A comparison of pixel-based and object-based classification at Nyamuragira volcano in the Democratic Republic of the Congo highlighted the advantages of the latter approach; it found that pixel-based classification of a lava surface results in more fragmented and heterogenous boundaries, while object-based classification resulted in more continuous and homogenous lava flow segments with clear boundaries and higher accuracy (Li et al., 2017-b; Rösch & Plank, 2022). The full potential of high-resolution data can be leveraged through an object-oriented approach that utilizes spectral and textural information, leading to improved lava flow classification compared to numerical modeling approaches such as MAGFLOW and LAHARZ (Rösch & Plank, 2022; Del Negro et al., 2008; Iverson et al., 1998).

2.5 Sensor Applications in Lava Flow Studies

The research papers that make up the 2020 Special Issue “Remote Sensing of Volcanic Processes and Risk” in the journal “Remote Sensing” show different ways remote sensing has been utilized in the context of studying volcanoes (Cigna et al., 2020). Together they show that remote sensing can be used to accurately capture the dynamics, magnitude, frequency, and impacts of volcanic activity in the ultraviolet (UV), visible (VIS), infrared (IR), and microwave wavelengths, and also show a trend in this field towards multi-data and multi-sensor monitoring (Cigna et al., 2020).

Data sources used in recent studies include, but are not limited to, optical imagery from Sentinel-2, thermal IR imagery from MODIS, Landsat-8, and ASTER, SAR imagery from TerraSAR-X, Sentinel-1, and Radarsat-2, and digital elevation models (DEMs) and surface models (DSMs) produced by airborne LiDAR and from stereo-derived products from spaceborne sensors such as Pleiades, SPOT 6/7, and PlanetScope (Cigna et al., 2020).

In the right conditions and with enough background contrast, high-resolution visible and near-infrared (VNIR) images, such as those produced by PlanetScope or Sentinel-2, can be used to create detailed lava flow maps showing structural and morphological changes associated with volcanic activity (Aldeghi et al., 2019; Cigna et al., 2020, Rösch & Plank, 2022). PlanetScope imagery has proven to be a reliable tool for lava flow mapping, showing strong agreement with validated false-colour time series from Sentinel-2 and Landsat 8 (Rösch & Plank, 2022). Although Sentinel-2 had a lower spatial resolution, its imagery was used for validation. This suggests that while PlanetScope allows for higher-resolution mapping, Sentinel-2 imagery remains valuable for mapping and monitoring volcanic hazards such as lava flows, ash, tephra deposits, and lahars, and for assessing classification accuracy (Rösch & Plank, 2022). Sentinel-2 was also used at Mount Kīlauea along with Landsat 8 imagery to delineate the active lava flow from the May 2018 Kīlauea–Leilani eruption, highlighting the value of Sentinel-2 for operational lava flow mapping in highly active volcanic areas (Musacchio et al., 2021).

Multiple studies have demonstrated the effectiveness of remote sensing for mapping and monitoring volcanic activity, particularly through the combination of optical and radar datasets.

Sentinel-2 optical imagery can be used successfully to differentiate between older and newer lava flows based on temporal change detection (Corradino et al., 2019), however, research has shown that integrating SAR with optical imagery enhances lava flow detection, especially in cloud-prone regions where optical data alone may be limited (Corradino et al., 2021). In these studies, the authors found that multi-sensor approaches using both radar and optical datasets, in combination with machine learning, led to more complete and accurate lava flow maps compared to single-sensor methods.

Further support for the value of multi-sensor approaches comes from research done at a variety of volcanic settings, such as Santorini, where Sentinel-1, Radarsat-2, and TerraSAR-X were used to analyze post-unrest ground deformation (Papageorgiou et al., 2019), and at Fuego Volcano, where the integration of Sentinel-1 and Sentinel-2 provided insight into morphological changes associated with lahar flows that would not have been possible using only one sensor type (Cando-Jácome & Martínez-Graña, 2019). Together, these studies indicate that combining different remote sensing data types improves mapping accuracy and monitoring capabilities by leveraging the complementary strengths of each sensor type.

2.6 SAR Capabilities

While SAR imagery is valuable for studying volcanic regions, recent research shows that the primary use of Sentinel-1 data has been to investigate surface deformation, with limited exploration of the use of SAR backscatter data for characterizing lava flow morphologies (Dabiri et al., 2023). Airborne Synthetic Aperture Radar (AIRSAR) L-band imagery with a wavelength of 24 cm can also be used to differentiate between types of lava flows (Tolometti et al., 2020). L-band imagery is sensitive to surface roughness at the decimeter scale (Carter et al., 2011; Neish & Carter, 2014), while C-band, such as for Sentinel-1, has a wavelength between 3.75-7.5 cm depending on the sensor (Ager, 2023, p. 4) and can capture finer surface roughness features, typically in the centimeters to decimeters scale (Tolometti et al., 2020).

Smooth surfaces, such as pāhoehoe flows, typically exhibit low circular polarization ratio (CPR) values (<0.5) due to single-bounce backscatter, while rougher surfaces, such as ‘a’ā flows, display moderate to high values (0.5–1.0) as a result of multiple-bounce backscatter (Tolometti et al., 2020). Blocky flows can produce CPR values exceeding 1.0 when double-bounce backscattering occurs on surfaces with natural corner reflectors, rock edges, and cracks (Campbell, 2012; Neish et al., 2016). These CPR patterns, derived from AIRSAR L-band data, have shown that while some morphological differences can be detected, even high-resolution optical data combined with CPR is not always sufficient to distinguish between morphologically similar surfaces like ‘a‘ā and rubbly pāhoehoe (Tolometti et al., 2020). C-band SAR, with its sensitivity to centimeter-scale roughness, has been hypothesized to capture distinct radar scattering properties between these subclasses of pāhoehoe and ‘a‘ā. However, this hypothesis remains uncertain, particularly in high-eruption-frequency areas (Tolometti et al., 2020).

2.7 Classification Variables

Lava flows can often be identified using a simple vegetation index such as NDVI, which highlights areas where vegetation has been removed or buried. However, this approach is only effective in vegetated regions and is less reliable near the crater where vegetation may be sparse or absent. In these cases, mapping unvegetated lava flows requires alternative methods. Darker lava flows can still be delineated using single spectral bands and appropriate reflectance thresholds (Aldeghi et al., 2019). As such, the spatial extent of lava flows can be determined through simple band operations using a combination of Sentinel-2's VIS and NIR bands.

The most common variables used in classification models for lava flow morphologies are spectral reflectance and surface roughness, as both are critical in distinguishing between pāhoehoe and ʻaʻā morphologies. Spectral reflectance, despite challenges associated with spectral similarity, can be used for lava flow classification (Al Shehri & Gudmundsson, 2019). For example, Sentinel-2 bands 2, 3, 4, and 8, with wavelengths of 492.4 nm (Blue), 559.8 nm (Green), 664.6 nm (Red), and 832.8 nm (NIR), have been used to discriminate between younger and older lava flows (Corradino et al., 2019).

Surface roughness, or surface texture, is an important distinguishing factor in lava flow morphologies. It reflects differences in surficial morphology between lava flow types and can be used to separate pāhoehoe, ʻaʻā, and blocky flows (Aufaristama et al., 2020). Roughness can be defined at various spatial scales, from the centimeter to meter scale, depending on the sensor and method used. Different lava types exhibit distinct textural characteristics across these scales, supporting the importance of roughness as a classification variable (Tolometti et al., 2020).

2.8 Surface Roughness Using SAR

Multiple methods used to derive surface roughness from SAR imagery exist. Variations in the backscatter intensity of the radar signal is one such variable that can be related to surface roughness. Rougher surfaces cause more diffuse scattering of radar signals, resulting in higher backscatter intensity values, as opposed to smooth surfaces that reflect radar signals away from the sensor and produce lower backscatter intensity values (Agar, 2023). Based on this backscatter interaction, we can assume that pāhoehoe lava flows should have lower backscatter intensities than ‘a’ā lava flows.

In addition to backscatter intensities, more advanced texture analysis techniques can be applied to SAR imagery to assess surface roughness. The Grey-Level Co-Occurrence Matrix (GLCM) is the foundation of one such method. GLCM characterizes spatial co-occurrence patterns of grey levels in imagery and can be used for the differentiation of geologically significant units such as pāhoehoe and ‘a’ā lava flows using SAR imagery (Gaddis et al., 1990). GLCM was used with field observations and roughness measurements at Mount Kīlauea to visually map out six lava flow morphologies: three pāhoehoe (ropy/shelly, sheet, and slab), transitional lava (spiny/rubbly pāhoehoe), and two 'a'ā flows (clinker and ball), found at the December 1974 flow along the South-west Rift Zone using L-band Space Shuttle Imaging Radar (SIR-B) imagery (Gaddis et al., 1990).

GLCM-derived statistics can be used to describe the textural features found in imagery, which can be correlated with surface roughness and used to differentiate between lava flow morphologies. These statistics can include but are not limited to: (i) *energy*, also known as *angular second moment*, measured as the degree of local homogeneity within the image’s grey level, reflecting textural uniformity, and focusing on partial characteristics of the given image. For instance, smoother surfaces have higher energy values due to their uniform texture resulting in more consistent grey-level patterns; (ii) *contrast*, measured as the difference in intensity between a pixel and its neighbours (local grey-level variation) over the whole image, reveals the clarity of the visual texture by extracting edge information of objects. This means the more textured a surface is, the higher the contrast value will be, representing rougher surfaces; (iii) c*orrelation*, measured as the linear dependency between the intensity values (grey tone) of a pixel and its neighbours, indicates how predictable those neighboring values are. High correlation occurs when pixel intensities are strongly related, often reflected in smoother, more uniform surfaces. Conversely, low correlation reflects less predictable relationships between the intensity levels, typical of rougher, more heterogeneous textures; (iv) *entropy*, measured as the degree of randomness/disorderliness in the grey-level distribution of pixel pairs. Higher entropy values indicate greater randomness and heterogeneity, suggesting rougher surfaces, and vice versa; (v) *homogeneity,* also known as *inverse difference moment*, is measured as the closeness of the distribution of pixel intensities in the diagonal, reflecting the extent of local variation in an image's texture. In other words, this measure reflects how similar neighbouring pixels are to each other. Higher homogeneity values indicate a lack of intensity variation between pixels, suggesting smoother surfaces (Gaddis et al., 1990; Mohamed & Lu, 2015; Hall-Beyer, 2017; Han et al., 2024).

While previous studies have demonstrated the value of SAR and optical imagery for mapping lava flow extents and differentiating between morphology types respectively, few have examined their combined potential for improving classification of lava flow morphologies. In particular, there has been limited exploration of how multi-sensor data and object-based image analysis can be used to distinguish between pāhoehoe and 'a'ā textures, especially in cases where transitional morphologies, such as rubbly pāhoehoe, complicate classification. This study addresses that gap through the combination of Sentinel-1 C-band SAR and Sentinel-2 optical imagery along with object-based image segmentation, to assess whether these can be used to enhance lava flow morphology classification accuracy beyond the current state of the art. This was done with a focus on Mount Kīlauea in Hawai'i, with particular attention given to differentiating between the most commonly encountered flow morphologies coming from basaltic eruptions: 'a'ā and pāhoehoe. This study evaluated a comparison of sixteen different band combinations, and six Segment Mean Shift (SMS) parameter sets using two labelling strategies, one based on morphology definitions and the other based on surface texture, to assess the impact of the transitional flow, rubbly pāhoehoe, on the accuracy of classification. Finally, for the highest-performing combinations for the two labelling strategies, GLCM texture features were extracted from segmented outputs to assess their utility for future unsupervised classification approaches. The design and implementation of this methodology are described in the following chapter.

Chapter 3. Research Design and Methodology

3.1 Study Area

Mount Kīlauea is monitored by the U. S. Geological Survey's (USGS) Hawaiian Volcano Observatory (HVO), founded in 1912 by Thomas A. Jaggar (Babb et al., 2011). Kīlauea is a basaltic shield volcano, characterized by a broad gently sloping profile, found on the southeastern shore of the island of Hawaiʻi (USA) above a hot spot in the central Pacific Ocean, and is the youngest of the volcanoes on the island (Sherrod et al., 2007).

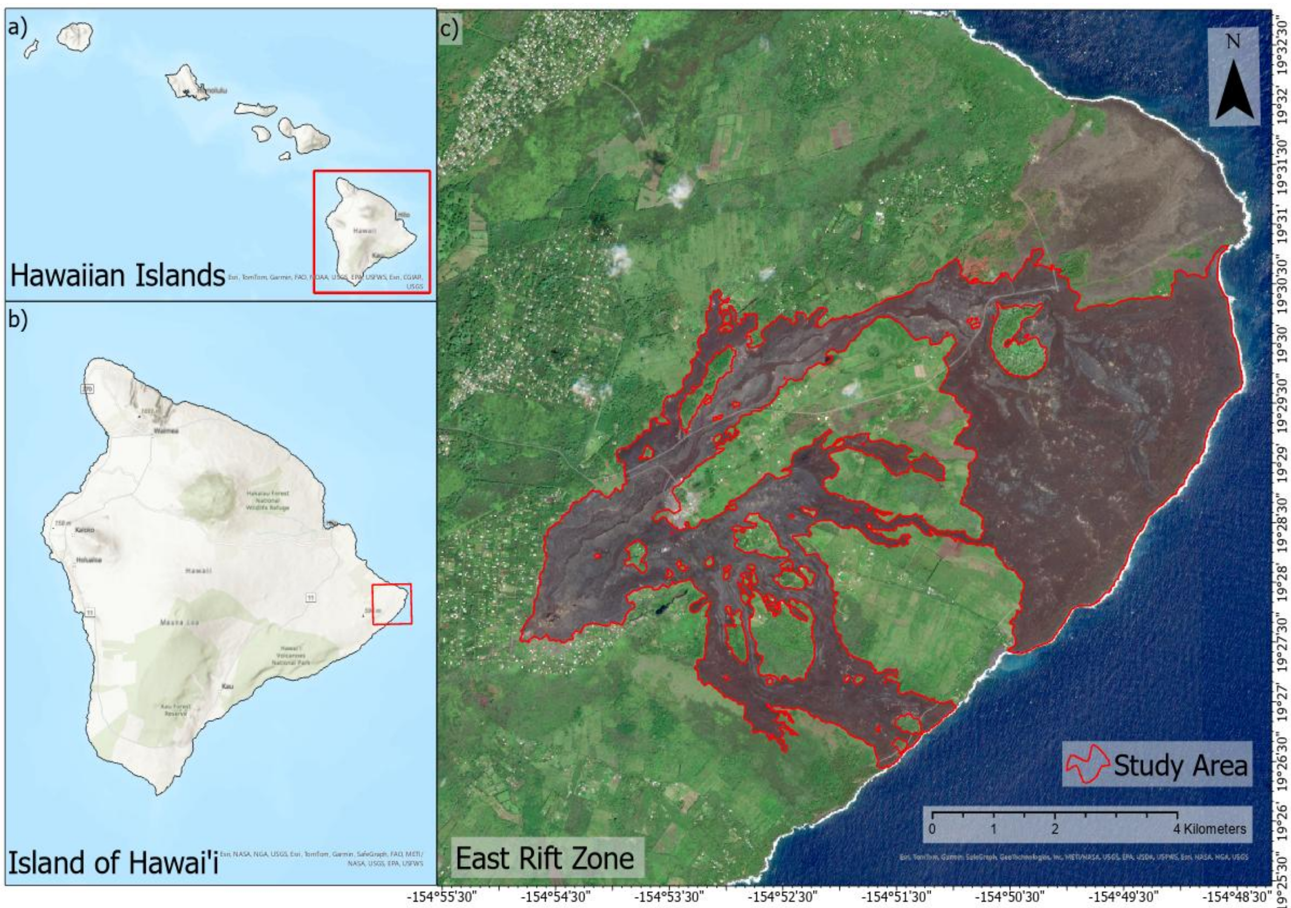

Figure 3. Study location map of the lava flow over the lower East Rift Zone on the Island of Hawai'i (Big Island). Outlined in red is the May-September 2018 eruption lava flow.

Lava flows younger than 1,000 years old cover 90% of the volcano due to its constant activity, with current research finding that the oldest flows found on the ocean floor are from eruptions that took place between 210,000 and 280,000 years ago (Sherrod et al., 2007; USGS, 2023). Mount Kīlauea is considered to be the most active, most accessible, safest, and best-studied volcano on Earth (Sheth, 2003), making it an ideal location to develop and test a lava flow classifier based on Sentinel-1 and Sentinel-2 imagery, as there are many recently emplaced lava flows that have not been affected by long term erosion. Mount Kīlauea is best known for its effusive eruptions, being called “the safest volcano on Earth” by HVO’s Thomas Jaggar (Babb et al., 2011). However, it does have a history of infrequent explosive eruptions that have left ash deposits. This has led the USGS and other scientists to believe that explosive eruptions occur about as often as explosive eruptions from volcanoes in the Cascade Range of the Pacific Northwest, such as Mount St. Helens (Mastin et al., 1999), with an average rate of twice per century during the past 4,000 years (Myers & Driedger, 2008).

Kīlauea's Puʻuʻōʻō eruption, on what is called the East Rift Zone (ERZ), started on January 3rd, 1983, and ended on April 30th, 2018, when the crater floor and lava lake collapsed. This made it the longest known eruption at just over 35 years, and the most voluminous eruption at this volcano, with ~4.4 km^3 of lava erupted during this period (Garcia et al., 2021). Many Hawaiian basaltic lava flows are pāhoehoe, and transition to ‘a’ā during the progression of the flow when the proper conditions (i.e., cooling, viscosity, and rate of shear strain) are met (Peterson & Tilling, 1980). 90% of basaltic flows are pāhoehoe or ‘a’ā, while the remaining 10% would fall into other categories such as blocky lava (Rowland & Walker, 1990).

After the Puʻuʻōʻō eruption ended, the magma started to drain away from the summit of Kīlauea into the middle and lower ERZ. The eruption found in the lower ERZ started on May 3rd, 2018, when fissures opened near the Leilani Estates residential subdivision, and officially ended on September 4th, 2018 (USGS HVO, 2018). According to the National Parks Service, this particular lava flow was responsible for destroying 700 homes, displacing over 2,000 people, covering ~48.3 km of road, and adding 875 acres of new land to the island (U.S. Department of the Interior, 2021). This lower ERZ lava flow is found in a generally accessible area and contains both pāhoehoe and ‘a’ā morphologies. The area has not undergone extreme weathering due to its young age, making it the ideal study location for this study.

3.2 Satellite Data Acquisition

This study used Sentinel-1 C-band SAR imagery (frequency 5.33 GHz, wavelength 5.6 cm) and Sentinel-2 optical imagery to support multi-sensor segmentation and classification of lava flow morphologies across the 2018 lower ERZ eruption at Mount Kīlauea, as well as to calculate GLCM texture features. These sensors were chosen due to their relatively high spatial and temporal resolutions, and their free and global availability. Sentinel-1 provides information on surface texture through radar backscatter, while Sentinel-2 offers high-resolution visible and near-infrared (VNIR) reflectance data suitable for spectral differentiation of lava types.

Imagery for this study was downloaded from Sentinel-Hub’s Earth Observation Browser. The Sentinel-1 imagery was captured using the Interferometric Wide Swath mode. The single and dual polarization layers VV and VH in linear gamma nought were acquired for both ascending and descending orbits. A cloud-free Sentinel-2 image was also downloaded, of which 4 bands (RGB and NIR) were used. The Sentinel-2 and Sentinel-1 descending orbit datasets were captured on February 12, 2020, and the Sentinel-1 ascending orbit datasets were capture on February 15, 2020. These dates were chosen as the closest available to the last eruption in the lower ERZ after allowing time for the lava flow to cool completely while avoiding the effects of long-term erosion. Using imagery from as small a time range as possible eliminates the risk of environmental change occurring between acquisitions, a real risk in high-eruption-frequency areas as they are subject to frequently changing landscapes over relatively short periods.

3.3 Validation Data

Field data, consisting of drone images taken on-site, were used to provide geolocated data for comparison to the satellite imagery classification results; all field data were used for validation, and none were used in the classification of the lava flows. Field data were collected February 08-18, 2024, on the Island of Hawai'i's lower East Rift Zone, using a DJI Mini 2 SE drone. A total of 390 images (Table 1) were captured over nine flights at six different locations within the study site (Figure 4). Due to technical limitations with the drone, flights were done manually without the help of a flight planner. However, manual flight planning was based on an existing lava flow classification for the lower ERZ, produced with field and helicopter reconnaissance data by the HVO (Patrick, unpublished data). Flight locations were selected to ensure that the drone would capture the different flow morphologies present in the study area, including variations of a'ā and pāhoehoe, and that flights could be conducted from safe and accessible take-off/landing positions.

Table 1. Field data information for imagery was collected in February 2024 using a DJI Mini 2 SE drone over the lower East Rift Zone on the Island of Hawai'i.

Location	Flight Number	# of Images	Drone Height at Liftoff (ft)	Conditions
1	1	41	50	Sunny
	2	59	100	
2	3	35	150	Sunny
	4	64	150	
3	5	50	150	Sunny
	6	43	150	
	7	22	150	
4	8	55	150	Sunny
5	9	21	150	Overcast/Windy

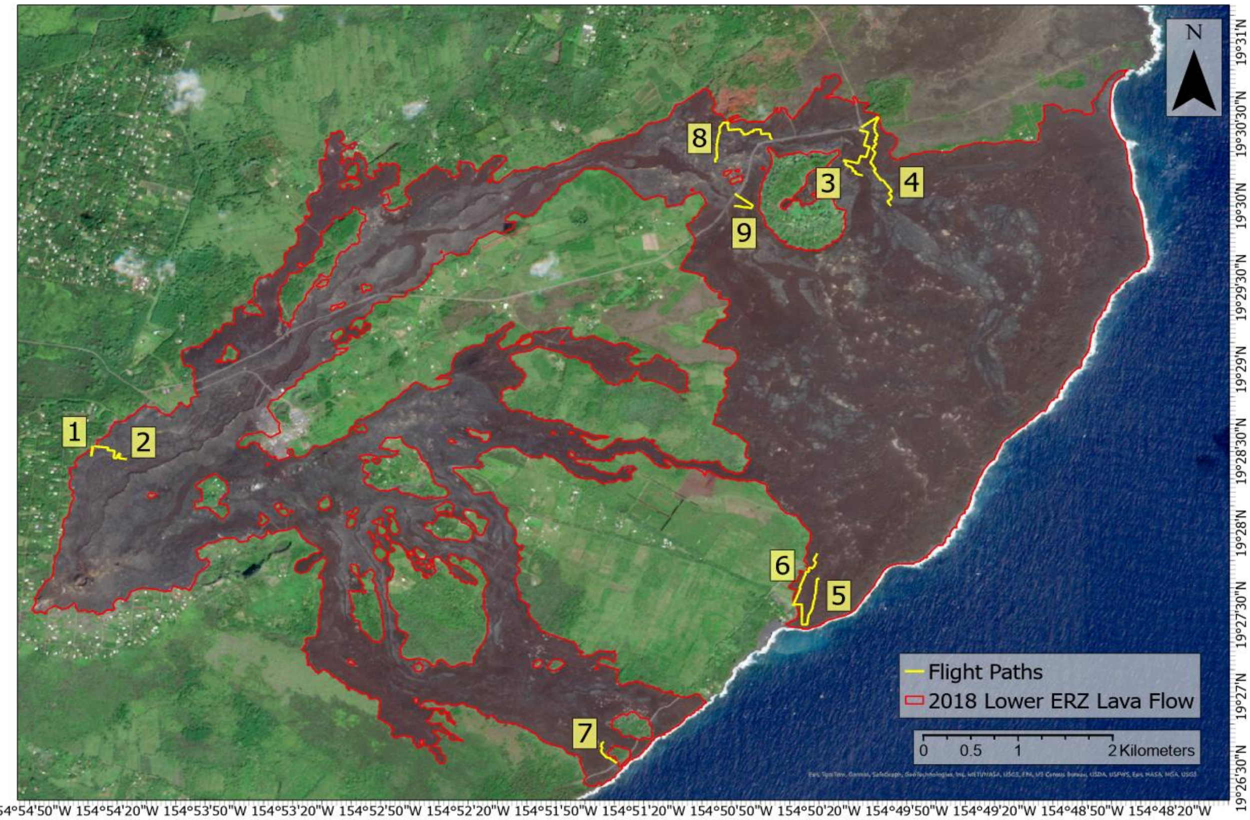

Figure 4. Flight path lines over the 2018 lower East Rift Zone (ERZ) lava flow. Numbered labels refer to the Flight Number column in Table 1.

Orthomosaics were generated from the drone imagery using ground control points from a LiDAR-derived DEM created specifically for the 2018 eruption area (Mosbrucker et al., 2020). The orthomosaics of each flight were then used to manually delineate polygons representing the two validation datasets: Definition (where rubbly pāhoehoe was grouped with pāhoehoe based on the common definition of the word) and Textural (where rubbly pāhoehoe was grouped with ʻaʻā to create groups with smooth vs. rough surface texture). Both *ʻAʻā* and *Pāhoehoe*, and *Smooth* and *Rough* polygons were drawn through visual interpretation of the drone-based orthomosaics. Lava flow boundaries were interpreted based on distinguishing morphological characteristics, including surface roughness, texture, and colour. In this thesis, pāhoehoe and ʻaʻā (lowercase) are used when referring to the morphologies as geological phenomena. When capitalized, or when similarly referring to Smooth and Rough, the terms denote the classification classes defined for this study.

Figure 5. Drone image captured during Flight 8 in February 2024. Dark brown areas represent 'a'ā and lighter grey areas represent pāhoehoe. The difference between the lava flow morphologies is made evident by the differences in surface roughness and colour.

Figure 6. Drone image captured during Flight 2 in February 2024. Dark brown areas on the right half of the image represent 'a'ā and lighter grey areas on the left half of the image represent rubbly pāhoehoe. In the Definition-based validation, the rubbly pāhoehoe was in the pāhoehoe class, while in the Textural-based validation, it was part of the rough class along with 'a'ā.

Figure 7. Drone image captured during Flight 3 in February 2024. Dark areas represent ‘a’ā and lighter grey areas represent pāhoehoe. The photo was taken at an angle to show the relative scale of the lava flow next to a forested area, as well as demonstrate the difference in reflectance between the two surfaces.

3.4 Lava Flow Classification

The following subsections detail the methods used to evaluate lava flow surface textures and generate segment-based classifications using multi-sensor (Sentinel-1 and Sentinel-2) satellite imagery. Most of the work was done in ArcGIS Pro v3.3.1 using *ModelBuilder* workflows, while Sentinel-1 SAR preprocessing was done in ESA’s SNAP software. The GLCM texture analysis was completed in Python in a JupyterLabs notebook.

3.4.1 Lava Flow Mask

A shapefile representing the lower ERZ 2018 lava flow field was created using ArcGIS Pro’s *spatial analysis* tools. Due to the lava flow ending in the ocean, the area following along the coastline of the island was used as the outer edge of the lava flow. To delineate the coastline, a water mask was created using the Modified Normalized Difference Water Index (MNDWI) using the Sentinel-2 bands 3 and 11, with a threshold of -0.2.

Equation 1. Modified Normalized Difference Water Index developed by Xu (2006).

$$MNDWI = \frac{(Green - SWIR)}{(Green + SWIR)}$$

Then, the Normalized Difference Vegetation Index (NDVI) was used to distinguish the lava flow from the surrounding vegetation, using a threshold of 0.3, to create a polygon delineating the extent of the lava flow using bands 8 and 4. This methodology is consistent with previous studies of basaltic lava fields (Al Shehri & Gudmundsson, 2019; Orynbaikyzy et al., 2023).

Equation 2. Normalized Difference Vegetation Index developed by Rouse et al. (1973).

$$NDVI = \frac{(NIR - Red)}{(NIR + Red)}$$

Finally, manual editing of misplaced vertices was done using the Sentinel-2 true-color image as a basemap. The result was exported as a shapefile to serve as the lava flow mask (red polygon seen on Figure 3).

3.4.2 Image Preprocessing

The Sentinel-1 imagery downloaded was already radiometrically terrain corrected (RTC), but speckle filtering was done in ESA's SNAP software using the Refined Lee speckle filter in the *Single Product Speckle Filter* tool.

The Sentinel-2 image acquired was Level 2A, indicating that it had already undergone orthorectification and atmospheric correction to derive surface reflectance values. The Sentinel-2 bands used in this study were the RGB bands (bands 2, 3, and 4), and the NIR band (band 8). These had been downloaded as 32-bit reflectance values.

The lava flow mask was then used to crop the Sentinel-1 and Sentinel-2 imagery to only include the lava flow pixels relevant to the classification, as well as to ensure that all bands were using the same extent.

3.4.3 Principal Component Analysis and Composite Bands

Prior to segmentation, 3-band composite images were needed for use in the Segment Mean Shift segmentation tool. In order to get as much spectral detail as possible in the composite images, a Principal Component Analysis (PCA) was applied to Sentinel-2 bands 2, 3, 4, and 8 to reduce spectral redundancy and maximize variance across the dataset. This transformation helped to compress the dimensionality of the input bands while preserving the key spectral differences relevant to lava surface characteristics. By reducing the correlated input bands and concentrating surface texture and reflectance variations into fewer components, PCA improved the separability of features during segmentation and minimized noise from redundant band information. PC1 and PC2 were prioritized when creating the multi-sensor composite images as they together accounted for over 98% of the total spectral variance across the four Sentinel-2 bands used. Specifically, PC1 explained 85.7% and PC2 explained 12.5%. Based on this, two multi-sensor approaches were applied: Multi-Sensor with a focus on Sentinel-2, where PC1 and PC2 were combined to a single Sentinel-1 band, and Multi-Sensor with a focus on Sentinel-1, where two SAR bands were combined with PC1.

A total of 16 unique 3-band composites (Table 2) were created using combinations of Sentinel-1 and Sentinel-2 bands to evaluate their effectiveness in segmenting lava flow morphologies. The analysis aimed to compare segmentation performance across optical-only, SAR-only, and multi-sensor combinations. The optical-only and multi-sensor combinations had 10 m pixels, with the 5-m Sentinel-1 bands being resampled to 10 m using nearest-neighbour interpolation to match Sentinel-2's resolution. However, in order to preserve spatial detail, the SAR-only combinations were kept at their native 5 m resolution.

Table 2. Band combinations used in the Segment Mean Shift segmentation model. Sixteen different combinations (C0-C15) were created from Sentinel-2 RGB and NIR bands (2, 3, 4, 8), principal components derived from those bands (PC1-PC3), and Sentinel-1 C-band backscatter in both VV and VH polarizations from ascending (ASC) and descending (DESC) orbits. These combinations were chosen to evaluate the relative performance of optical, radar, and multi-sensor inputs for segmenting lava flow textures.

Combination ID	Description	Band 1	Band 2	Band 3
C0	Sentinel-2 RGB	2	3	4
C1	Sentinel-2 Principal Components	PC1	PC2	PC3
C2	Sentinel-1 ASC only (VH focus)	VH_ASC	VH_ASC	VV_ASC
C3	Sentinel-1 ASC only (VV focus)	VH_ASC	VV_ASC	VV_ASC
C4	Sentinel-1 DESC only (VV focus)	VV_DESC	VH_DESC	VV_DESC
C5	Sentinel-1 DESC only (VH focus)	VV_DESC	VH_DESC	VH_DESC
C6	All Sentinel-1	VV_ASC	VH_ASC	VH_DESC
C7	All Sentinel-1	VV_ASC	VV_DESC	VH_DESC
C8	Multi-sensor (S1 focus)	PC1	VV_ASC	VH_ASC
C9	Multi-sensor (S1 focus)	PC1	VV_DESC	VH_DESC
C10	Multi-sensor (S1 focus)	PC1	VV_ASC	VV_DESC
C11	Multi-sensor (S1 focus)	PC1	VH_ASC	VH_DESC
C12	Multi-sensor (S2 focus)	PC1	PC2	VV_ASC
C13	Multi-sensor (S2 focus)	PC1	PC2	VH_ASC
C14	Multi-sensor (S2 focus)	PC1	PC2	VV_DESC
C15	Multi-sensor (S2 focus)	PC1	PC2	VH_DESC

3.4.4 Segmentation

The next step was to segment the lava flow into classes using the SMS tool. This tool groups pixels into segments based on spatial coherence and similarity in spectral and spatial characteristics. Six different parameter sets were tested (Table 3) to find the best combinations for the Definition- and Textural-based classes, with only the spatial detail value changing. The Spatial detail parameter defines the level of importance given to the proximity between features in the imagery, meaning larger values emphasize small, closely spaced features, while smaller values create smoother, more generalized segments (ESRI, n.d.). Spectral detail values below 20 did not produce good segmentation results, so this was kept as a fixed value. Minimum segment size of 10 pixels was also fixed to prevent over-segmentation, ensuring only meaningful spatial patterns are retained while still being small enough to capture transitional zones where rubbly pāhoehoe is found. This meant that the results of the SMS tool generated many (>100) small segments across the lava flow.

Table 3. Segment Mean Shift parameter sets used for image segmentation. Each set varies the spatial detail parameter while keep spectral detail (20) and minimum segment size (10 pixels) constant.

Param Set ID	Spectral Detail	Spatial Detail	Min Segment Size (pixels)
P1	20	18	10
P2	20	16	10
P3	20	14	10
P4	20	10	10
P5	20	5	10
P6	20	1	10

3.4.5 Multivariate Clustering

The segments created by SMS were then grouped into 4 clusters using the *Multivariate Clustering* tool. This number of clusters was chosen after having visually examined the results of using 2, 3, 4, or 5 clusters, as it produced the best segmented results. The clustering method used was K-Means, and the analysis fields were the mean values of the 3 bands used in the respective segmented composite image. Some of the 16 band combinations consistently produced poor results and were thus omitted from further evaluation. These included: C4, C5, C6, C7, C9, C11, and C12 (Table 2). Of the band combinations excluded, 6 of the 7 included the descending orbit Sentinel-1 data. Because both the Definition-based (Pāhoehoe vs. ʻA'ā) and Textural-based (Smooth vs. Rough) classifications are binary (based on two classes), manual merging of the 4 cluster groups to 2 clusters was done. The clusters were merged based visual examination of the Sentinel-2 image and my knowledge of the study site's lava flow morphologies.

3.4.6 Classification Validation

The Definition- and Textural-based validation polygons were overlaid on the classified results from each band combination/parameter set to calculate the proportion of accurately classified areas for both lava classes. Overall Accuracy (OA) was calculated by dividing the total correctly classified area by the total area; then for each lava flow type, User Accuracy (UA) was calculated by dividing the correctly classified area for the respective class by the total area labeled as that class, and Producer Accuracy (PA) was calculated by dividing the correctly classified area for the respective class by the total reference area for that class. F1 Scores were also calculated to provide a balanced measure of classification performance, representing the harmonic mean of UA and PA.

3.4.7 Grey-Level Co-Occurrence Matrix Features

GLCM texture features were tested to see if they could be used to quantify surface texture and help automate class labeling to reduce manual work. The features included: contrast, homogeneity, energy, and entropy.

The values for contrast and entropy range from 0 to ∞, meaning they can have very high values depending on image intensity and texture. Contrast values close to 0 represent low local grey level variation, whereas higher values reflect greater variation. This means that the rougher a surface gets, the higher the contrast value will get. The same is true for entropy, where a value close to 0 represents uniform texture (no randomness), and becomes higher the more complex and varied a surface texture becomes.

The values for homogeneity and energy, however, range from 0 to 1 as these are normalized measures. For the former, a value of 0 means high variability in pixel values (low homogeneity), while 1 means similar pixel values throughout the segment (high homogeneity). Contrarily to entropy, energy values closer to 0 represent high randomness (low uniformity), while 1 represents very uniform texture (high uniformity).

The band combinations with the most accurate results for the Definition- and Textural-based classifications were used to calculate the four GLCM features. The four features were computed per segment using a custom Python function leveraging the *scikit-image* library, which applied co-occurrence matrix analysis on the spatial layout of pixel values within each polygon.

The GLCM calculations were based on the methods and descriptions provided by Gaddis et al. (1990), Mohamed & Lu (2015), Hall-Beyer (2017), and Han et al. (2024), using a distance of one pixel and angles of 0°, 45°, 90°, and 135° to capture texture in multiple directions. This was done for each band of the selected composite images. Each class polygon was used as a mask to extract only the pixels within its bounds, and values were scaled to an 8-bit (0-255) greyscale range to allow for discrete GLCM generation.

The below equations were used in the Python function as follows: let P(i, j) be the normalized co-occurrence matrix entry at row i, column j, with N grey levels.

Equation 3. GLCM texture feature Contrast. Measures local variation in intensity:

$$\text{Contrast} = \sum_{i=0}^{N-1} \sum_{j=0}^{N-1} (i-j)^2 \cdot P(i,j)$$

Equation 4. GLCM texture feature Homogeneity. Measures similarity of neighboring pixel values (inverse contrast):

$$\text{Homogeneity} = \sum_{i=0}^{N-1} \sum_{j=0}^{N-1} \frac{P(i,j)}{1+|i-j|}$$

Equation 5. GLCM texture feature Energy (Angular Second Moment). Measures uniformity (squared sum of co-occurrence probabilities):

$$\text{Energy} = \sum_{i=0}^{N-1} \sum_{j=0}^{N-1} [P(i,j)]^2$$

Equation 6. GLCM texture feature Entropy. Measures randomness or disorder. ε is a small value (e.g., $\varepsilon = 1 \times 10^{-10}$) used to avoid log(0):

$$\text{Entropy} = -\sum_{i=0}^{N-1} \sum_{j=0}^{N-1} P(i,j) \cdot \log_2 \left(P(i,j)+\varepsilon\right)$$

For each band within a polygon, the texture features were computed from the normalized GLCM using these standard formulas. The texture features for all bands were averaged to produce a single set of values per segment. Finally, the results were grouped by morphology class (A‘ā’ or Pāhoehoe, Smooth or Rough) to compare class-level average texture statistics. This approach ensured that the analysis was sensitive to both the spectral content of the imagery and the spatial structure of the surface textures within each segment.

3.5. Statistical Analysis of Terrain Variables

In order to evaluate the effects of slope and aspect on classification performance, a 1-m resolution LiDAR-derived DEM created in 2019 to capture the lower ERZ eruption (Mosbrucker et al., 2020) was used. Spatial Analyst tools in ArcGIS Pro were used to create slope and aspect layers based on this DEM. These terrain layers, together with Sentinel-2, Sentinel-1, and multi-sensor classification result layers, were exported and analyzed in Python.

Because aspect is a circular variable (0° and 360° represent the same direction), it was transformed into two continuous variables based on trigonometric decomposition (Roberts, 1989):

$$Northness = \cos(Aspect\ in\ radians)$$

$$Eastness = \sin(Aspect\ in\ radians)$$

Northness and Eastness values range from -1 to 1, with values close to 1 representing north/east-facing slopes and -1 representing south/west-facing slopes respectively (Das et al., 2025).

To first evaluate the effects of terrain on the classification results, normality was tested using the Shapiro-Wilk test (Tak et al., 2023). The three variables (slope, Northness, and Eastness) were tested, and resulted in p-values < 0.05, confirming that none of the data were normally distributed. As a result, the Mann-Whitney U test was applied, and effect sizes were calculated using Cliff’s Delta function. The Mann-Whitney U test is a non-parametric statistical test used to determine whether two independent groups (in this case: correctly classified vs. misclassified polygons) differ significantly in their distributions, without assuming that the data being evaluated follow a normal distribution (Mann & Whitney, 1947). In this study, the test was applied separately to each terrain variable to assess whether the distribution of these variables differed between the sensor groups, as well as between the classes within each group. Alongside this, the Cliff's delta is commonly interpreted using thresholds to determine whether the effect size was "negligible", "small", "medium", or "large" (Meissel & Yao, 2024). For my study, the default thresholds suggested by Cohen (1988) were used: negligible ≤ 0.10, small > 0.10 to < 0.33, medium ≥ 0.33 to < 0.47, and large ≥ 0.47. This approach was used for each of the three sensor-group band-combination result layers to evaluate whether terrain variables contributed to classification errors, as well as on a class-level to evaluate how the terrain variables may affect one class over the other. These tests were done on the best-performing classification results for the Description-based validation methods per main sensor group, Sentinel-1 (C2_P5), Sentinel-2 (C0_P6), and multi-sensor (C13_P5) (see Tables 2 and 3).

Chapter 4. Results

In this section, the accuracy assessment of the best band combinations (Table 2) and parameter sets for the SMS model (Table 3) for the classification of 'A'ā and Pāhoehoe/Rough and Smooth lava flow morphologies is covered. In addition, the usefulness of GLCM texture metrics to support a more unsupervised method of labeling segments is evaluated, as well as the effects of terrain on the classification results.

All of the classification accuracies presented here were calculated using the validation polygons manually digitized from the high-resolution drone imagery orthomosaics. These orthomosaics were never used in segmentation or clustering; they served only as independent reference data for accuracy assessment. The reported Overall Accuracy, User Accuracy, Producer Accuracy, and F1-Scores reflect comparisons between the satellite-based classifications and the drone-derived ground truth imagery.

4.1 Overall Classification Accuracy

The overall accuracy (OA) for each band combination group used can be found in Table 4, with the complete results table found in Appendix 1. The highest OA for the Definition-based classification, meaning the classification of pāhoehoe and ‘a’ā based on their common definitions, was produced by the multi-sensor band combination using Sentinel-2’s principal components 1 and 2, and Sentinel-1’s VH band from the ascending orbit (C13 in Table 2), with either the 4th or 5th parameter set (P4 and P5 in Table 3) used in the SMS model. The overall accuracy for C13_P4/P5 was 86.31% (Table 4). The second-most accurate was the Sentinel-2 band combination C0 (the RGB bands; Table 2) using the P6 parameter set (Table 3); this combination was 0.25 percentage points lower in overall accuracy. The highest OA for the Textural-based classification, the classification of Smooth and Rough lava where rubbly pāhoehoe was grouped with ‘a’ā), was produced by the Sentinel-2 band combination C0, with the P6 parameters. The OA of this band-parameter combination was 88.69%, with the second-most accurate being C13 with the P4 parameters with an OA of 87.8%. These results indicate that lava flow morphology classification, overall, has 2.38 percentage points higher OA when basing the classes on surface roughness rather than their common definitions.

When comparing the results within each band combination group, it is also important to note that although the best performing Sentinel-1 band combinations produced results that are less accurate than those derived from Sentinel-2 or multi-sensor combinations, the results are still accurate enough to support meaningful classification in the event optical data is unavailable; with both classification methods having OAs of ~77%, comparable to other SAR-based lava flow mapping methodologies (Balaguera et al., 2023).

Table 4. Overall Accuracy (OA) results for the best-performing band combinations (Table 2) and parameter sets (Table 3) in each band combination group tested: Sentinel-2, Sentinel-1, and multi-sensor approaches combining Sentinel-1 and Sentinel-2. Highest OA for both classification types are in bold.

Band Combination Group	**Definition-Based Classification**		**Textural-Based Classification**	
	Combination and Parameter Set ID	**Definition OA (%)**	**Combination and Parameter Set ID**	**Textural OA (%)**
Sentinel-2 - Optical	C0_P6	86.06	**C0_P6**	**88.69**
Sentinel-1 – SAR	C2_P5	76.91	C3_P6	77.30
Multi-Sensor (Sentinel 1 focused)	C8_P2	82.37	C8_P1	84.27
Multi-Sensor (Sentinel 2 focused)	**C13_P4 / C13_P5**	**86.31**	C13_P4	87.80

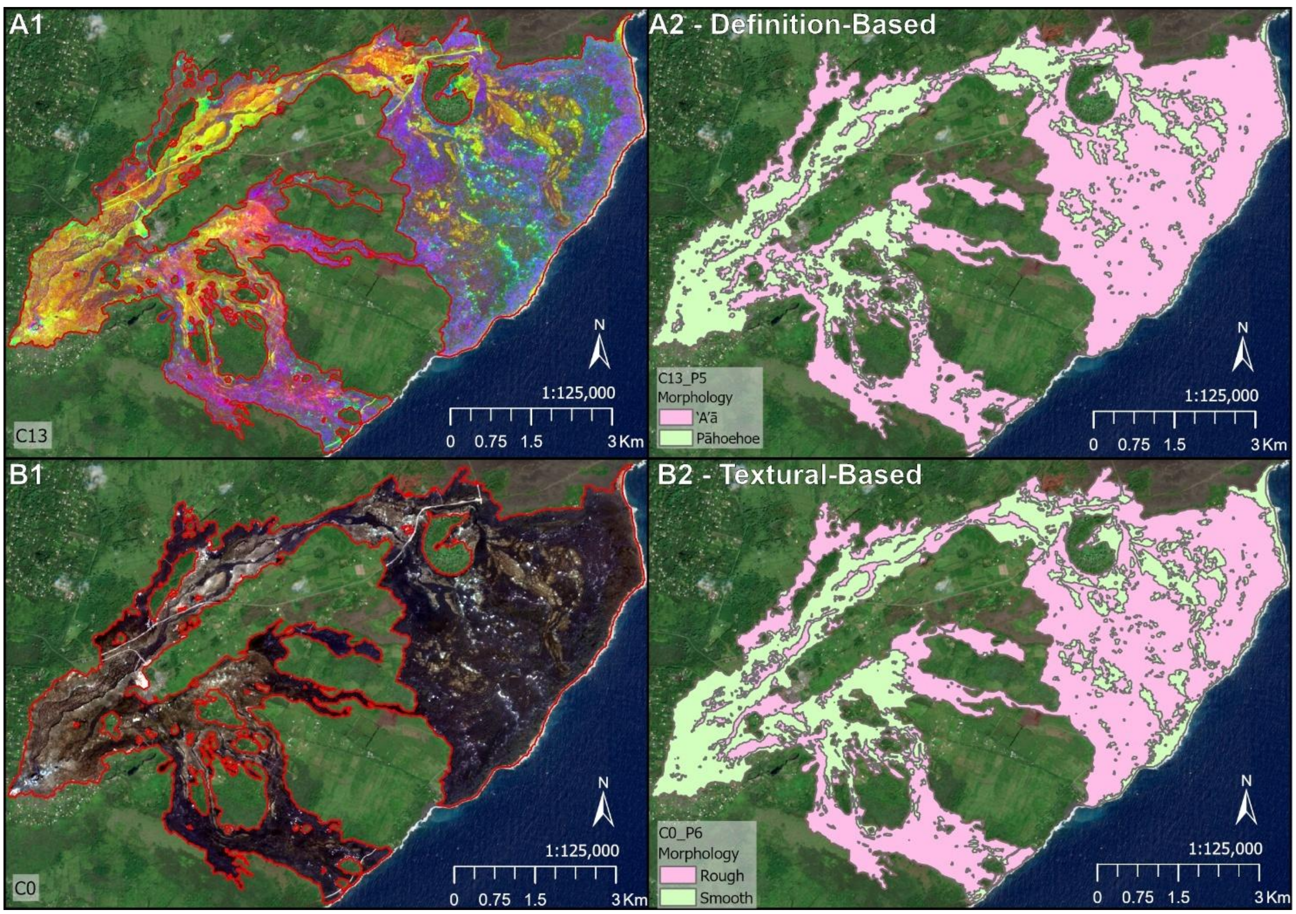

Figure 8. Results of object-based lava flow classification for the 2018 lower East Rift Zone (ERZ) eruption, Hawai'i., using Sentinel-1 and Sentinel-2 imagery. Panels A1 and B1 represent the band combinations C13 and C0 respectively. The C13 false colour composite uses Sentinel-2's PC1 and PC2, and Sentinel-1's

VH_ASC. The C0 composite uses Sentinel-2's RGB bands 2, 3, and 4. Panels A2 and B2 show, respectively, the 'A'ā and Rough classes in light pink, and the Pāhoehoe and Smooth classes in green.

4.2 Class-Based Accuracy Metrics

Table 5 summarizes the User Accuracy (UA), Producer Accuracy (PA), and F1 Score for each class under the best-performing Definition-based (C13_P5) and Textural-based (C0_P6) classification scenarios (see Figure 8). First, it should be noted that the classes are imbalanced; the A'ā and Rough classes each contain more than twice the number of pixels compared to the Pāhoehoe and Smooth classes (Appendix 3), representative of the 2018 lower ERZ flow being dominated by 'a'ā. Overall, the Textural-based classification performed better than the Definition-based classification for each of their classes. Textural-based classification resulted in a higher UA for the Rough class, indicating that the Rough class had 3.4 percentage points fewer false positives than the 'A'ā class. Similarly, the higher PA for both classes indicates that Textural-based classification captured more true pixels than Definition-based, with Rough having 0.99 percentage points fewer false negatives than 'A'ā, and Smooth having 2.93 percentage points fewer false negatives than Pāhoehoe. The higher F1 Scores also indicate better balance between UA and PA for both classes in the Textural-based classification.

Pāhoehoe's PA was 17.32 percentage points lower than 'A'ā, and Smooth's PA was 15.38 percentage points lower than Rough, indicating that a substantial proportion of actual Pāhoehoe/Smooth areas were not correctly identified. Again, it is important to note that Pāhoehoe and Smooth classes are underrepresented, however, the validation data was representative of the entire mapped flow and therefore captures this natural class imbalance.

Table 5. Accuracy metrics calculated for the best-performing Definition-based (C13_P5) and Textural-based (C0_P6) classification methods. Accuracy metrics include User Accuracy (UA) and Producer Accuracy (PA)l in percentages, and F1 Score, where a score of 1 indicates perfect agreement.

Accuracy Metric	Definition-Based Classification		Textural-Based Classification	
	‘A’ā	Pāhoehoe	Rough	Smooth
UA (%)	86.36	86.26	89.76	86.19
PA (%)	92.79	75.47	93.78	78.40
F1 Score	0.89	0.81	0.92	0.82

These results also highlight differences between the sensor groups. For Definition-based classification, the C13 combination (Sentinel-2 PC1, PC2 + Sentinel-1 VH ascending) produced higher accuracy, while for the Textural-based classification, the best results came from the C0 combination using only Sentinel-2 bands. For Definition-based classification, the overall best-performing combination was C13 followed by C0, while for Textural-based, C0 was the best-performing combination followed by C13.

The second-best performing combinations (Definition-based C0_P6 and Textural-based C13_P4) followed the same trend as the best-performing ones, with slightly lower OAs. Of note, the multi-sensor Textural-based combination had a slightly more balanced performance between Rough and Smooth classes, suggesting that a minor reduction in OA can be acceptable when the goal is to improve classification of underrepresented classes. The detailed accuracy metrics for these combinations are provided in Appendix 2.

4.3 GLCM Texture Analysis

The average GLCM texture metrics, contrast, homogeneity, energy, and entropy were calculated for the best-performing classification results’ two classes (Table 7). The assumption was that ‘A’ā/Rough would be characterized by high contrast, low homogeneity, low energy, and high entropy, whereas Pāhoehoe/Smooth was expected to have low contrast, high homogeneity, high energy, and low entropy. The results aligned with these expectations.

Table 6. Average GLCM texture values and percent differences between 'A'ā and Pāhoehoe for the best-performing band combinations in each classification method. Percent differences are calculated relative to the Pāhoehoe value, with positive values indicating higher values in A'ā'.

GLCM Texture Metric	Definition-Based Classification			Textural-Based Classification		
	'A'ā	**Pāhoehoe**	**% Difference**	**Rough**	**Smooth**	**% Difference**
Contrast	242.42	114.21	+112.26	16.61	9.02	+ 84.15
Homogeneity	0.79	0.91	-13.19	0.85	0.91	- 6.59
Energy	0.73	0.87	-16.09	0.75	0.85	- 11.76
Entropy	14.44	6.65	+117.14	10.56	6.82	+ 54.84

The degree of separation between 'A'ā and Pāhoehoe's values for contrast and entropy are the most pronounced, with 'A'ā having more than double the values of Pāhoehoe for these metrics. Homogeneity and energy have smaller, but still clear differences. For the Rough and Smooth classes, this pattern remains though with slightly lower percent differences. For entropy, the percent difference between classes was substantially lower in the Textural-based classification (Rough being 54.84% larger than Smooth) compared to the Definition-based classification (where 'A'ā was 117.14% higher than Pāhoehoe), meaning there is a smaller separation in average entropy values between the two texture classes, indicating the potential sensitivity of this metric to transitional lava flows (in this case rubbly pāhoehoe). Overall, the consistent trend across metrics for both Definition- and Textural-based approaches suggests that these are stable indicators of surface roughness and are therefore promising candidates for use in unsupervised or semi-supervised classification workflows.

4.4 Effects of Terrain on Classification Results

The Shapiro-Wilk normality test results showed that all variables (slope, Northness, and Eastness) had a $p < 0.05$, indicating non-normal distributions, and thus supporting the use of non-parametric tests. The results of the Mann-Whitney U test and the Cliff's Delta effect size interpretations are found in Table 8. The terrain variables most likely to have had a meaningful effect on classification have both low p-values and non-negligible Cliff's Delta values.

Table 7. Overall results of the Mann–Whitney U test and Cliff's Delta effect size for terrain variables (slope, Northness, Eastness) across correctly classified and misclassified polygons for each sensor group, using the Definition-based validation method. Statistically significant p-values ($p < 0.05$) in bold indicate a significant difference in the distribution of the variable between the two classification outcomes. Cliff's Delta values describe the magnitude and direction of the effect, with positive values indicating higher effects on correctly classified polygons, and negative values indicating higher effects on misclassified polygons.

Sensor Group	Variable	p-value	Cliff's Delta	Effect Size
C0_P6 Sentinel-2	Slope	0.6806	-0.0413	negligible
	Northness	**2.45e-06**	**-0.3714**	**medium**
	Eastness	0.0943	-0.1671	small
C2_P5 Sentinel-1	Slope	0.9724	0.0028	negligible
	Northness	0.6255	-0.0385	negligible
	Eastness	0.9044	-0.0095	negligible
C13_P5 Multi-Sensor	Slope	0.0517	-0.1883	small
	Northness	**0.0016**	**-0.3055**	**small**
	Eastness	0.5594	0.0566	negligible

For Sentinel-2 (C0_P6) data, classification accuracy was significantly influenced by Northness (p = 2.45e-06, with a medium effect), meaning misclassified polygons tend to occur more on north-facing slopes. For Sentinel-1 (C2_P5), slope, Northness, and Eastness all had negligible, non-significant effects. Finally, for the multi-sensor (C13_P5) data, Northness again appears to be a significant factor (p = 0.0016, small effect), though the effect is not as strong as for the Sentinel-2-only group. Slope approached significance (p = 0.0517), though with a small effect.

Chapter 5. Discussion

The classification results from the Sentinel-1 SAR, Sentinel-2 optical, and the multi-sensor (SAR + optical) band combinations provide insight into the strengths and limitations of each sensor in differentiating the two most common basaltic lava flow morphologies, ʻaʻā and pāhoehoe. Through the use of two validation methods, Definition-based and Textural-based, an evaluation of the difference between classifying the transitional lava flow rubbly pāhoehoe as Pāhoehoe (Definition) or as Rough (Textural) was done. Additionally, the effects of terrain on classification results were evaluated.

5.1 Classification Results

The testing of different band combinations and parameter sets for use in object-based classification produced robust accuracy outcomes, allowing for a detailed comparison across sensors and validation approaches. Overall, the use of SMS followed by K-Means clustering successfully distinguished lava flow morphologies with accuracies on the order of 85-89%, with some variation between the Definition-based and Textural-based validation methods.

In the Definition-based classification (classes based on common definitions), the highest OA was 86.31% using a multi-sensor band combination consisting of Sentinel-2 principal components 1 and 2, and the Sentinel-1 VH band from the ascending orbit path. This outperformed single-sensor band combinations, though the second-best performance was Sentinel-2 bands 2, 3, and 4 with an 86.06% OA (Appendix 2). Contrarily, for the Textural-based classification (Smooth vs. Rough), the best accuracy was slightly higher, with an 88.69% OA using only the three Sentinel-2 RGB bands. Similarly to the Definition-based results, this was only 0.89 percentage points higher in overall accuracy than the PC1+PC2+VH multi-sensor band combination. In general, classifying lava flows based on surface texture resulted in 2.38 percentage points higher OA than using the common pāhoehoe and ‘a’ā definitions, suggesting that grouping flows by roughness provides a clearer spectral-textural separation in imagery, likely because it reduces the confusion between transitional morphologies.

Despite the high accuracies, the results revealed some consistent bias towards the over-classification of the Rough/‘A’ā classes. The Smooth/Pāhoehoe classes consistently showed higher omission errors than the Rough/‘A’ā classes. In the best classifications, the PA for Smooth/Pāhoehoe were between ~75-78%, while the PA for Rough/‘A’ā were between 92-94%. This means that a relatively larger portion of the actual Smooth/Pāhoehoe areas were not correctly classified (omitted), while the vast majority of actual Rough/‘A’ā were correctly labeled as such. Part of this difference is caused by the underlying class imbalance, as Rough/‘A’ā covers more than twice the area of Smooth/Pāhoehoe. This imbalance is not the result of a sampling artifact, but a reflection of the true proportions of flow morphologies in the 2018 lower ERZ eruption. Larger classes generally have higher producer accuracies, because there are more reference samples available and fewer opportunities for omission errors to strongly affect the percentage (Albattah & Khan, 2025; Zhang et al., 2023). Thus, this imbalance amplifies the difference in PA between the classes.

This imbalance compounds the effect of textural differences between the two morphologies, where parts of the pāhoehoe flow that are rougher on the larger dm-scale get grouped into the rougher class. Additionally, mixed pixels are more likely to be classified as Rough/‘A’ā since rougher textures tend to dominate spectral variance in optical data as well as in radar backscatter (Dierking, 2002; Purinton & Bookhagen, 2020; Zhang et al., 2020), meaning more omission errors of the smoother classes. In SAR, jagged surfaces scatter more strongly and irregularly, while in optical imagery, rougher flows appear darker and more variable due to shadowing and microtopography (e.g. small ridges, cracks, fissures, etc.), making them more spectrally distinct than the smoother pāhoehoe (Gaddis et al., 1990).

This is also made evident by the difference in F1 Scores between Definition- and Textural-based classifications. The Textural-based F1 Scores are consistently higher, indicating a better-balanced performance when grouping rubbly pāhoehoe in with the Rough class. Conversely, the UA differences between classes are smaller, with all UA values across the best-performing Definition- and Textural-based classifications being between 86-90%. Together, these results suggest that classification tends to over-predict Rough/‘A’ā and under-predict Smooth/Pāhoehoe. While this bias reflects spectral/textural differences, it is strengthened by the class imbalance in the data. This bias is systematic across band and parameter combinations for both optical and SAR, suggesting that it could potentially be corrected in post-classification adjustments.

5.1.1 Sensor Comparison

The performance of the classification varied between sensor band combination groups. Sentinel-2 optical imagery proved to be highly effective at differentiating lava flow morphologies, outperformed Sentinel-1 by ~10 percentage points in OA. This can be attributed to the distinct differences in surface reflectance between the rougher ‘a’ā, which appears darker on optical imagery, and the smoother pāhoehoe, which appears lighter on imagery. The lower performance from SAR is not unexpected, as C-band radar backscatter can be less sensitive to textural differences smaller than its wavelength, as well as speckle noise inherent in SAR imagery which can obscure small scale texture patterns. This aligns with the findings of other studies who found that mapping ‘a’ā lava flows was more effective than pāhoehoe (Corradino et al., 2021; Gaddis et al., 1990). Nevertheless, Sentinel-1’s ~77% accuracy using either a combination of mostly VH bands (C2_P5, Definition-based), or mostly VV bands (C3_P6, Textural-based), all in ascending orbit, is still meaningful for classification when optical data are unavailable for extended periods of time and mapping of lava flows needs to be done in a timely manner during active events. In this study, the best multi-sensor combination generally matched the highest accuracy optical combination, suggesting that in ideal imaging conditions, high-quality optical imagery alone is sufficient for differentiating lava flow morphologies. The addition of Sentinel-1 data did not produce statistically meaningful improvements in overall accuracy at this study site, indicating that the benefit of a multi-sensor approach is limited when clear optical imagery is available. However, the use/addition of SAR data could contribute more meaningfully to operational contexts, when time-sensitive mapping is needed, or for areas with very persistent cloud cover. Regardless of cloud cover, ash plumes, or time of day, this object-based approach can still classify flow morphologies with a reasonable degree of reliability using SAR only. Additionally, SAR could be used to compliment optical imagery where some areas are covered by clouds by fusing the data sources over these areas.

5.1.2 Parameter Tuning

This study's object-based segmentation using the Segment Mean Shift algorithm and subsequent K-Means clustering, proved to be effective across a range of segmentation parameters. Six parameter sets were tested using different levels of spatial detail importance. Based on the results, the highest accuracies tended to be on the finer end of the scale tested, with P4, P5 and P6 (spatial detail of 10, 5, 1 respectively). When comparing the results of all the tests done (see Appendix 1), it is clear that the SMS algorithm is generally robust, with most accuracies only varying by a few percentage points between different parameter sets. Spectral detail values below 20 consistently produced worse results (not shown), hence this parameter was fixed in this study. These results suggest that segmentation is not very sensitive to spatial detail, but that relatively low values of spatial detail could be used by default when applying this workflow to other locations.

5.1.3 GLCM Texture Metrics Insights

Analyzing the Grey-Level Co-Occurrence Matrix (GLCM) texture metrics for the best-performing classifications provides insights into the physical surficial differences between lava flow morphologies and how these metrics can potentially be used to enhance unsupervised classification techniques. As expected, the Rough/'A'ā surfaces have higher contrast and entropy values than the Smooth/Pāhoehoe surfaces, while the latter had higher homogeneity and energy values. These results align perfectly with the assumptions made, especially with regard to the Definition-based classification. The average contrast and entropy of 'A'ā segments being more than double that of Pāhoehoe reflects the fact that 'a'ā lava is considered rough at both the small (centimeter to decimeter) scale and the large (meter) scale (Whelley, 2017), creating highly variable pixel intensity values with high local variance between adjacent pixels. This high local variance in 'a'ā segments reflects abrupt changes in brightness between neighboring pixels, indicating a complex and irregular microtopography. Meanwhile, pāhoehoe, including rubbly pāhoehoe, is smoother at the cm-scale than 'a'ā, and has a more uniform crust and ordered texture, characterized by low contrast and low entropy (see Figures 5 and 6).

The Textural-based classification showed the same overall pattern of contrast/homogeneity/energy/entropy differences, confirming that the Rough class is consistently distinguishable from the Smooth class. However, the degree of separation in GLCM values was lower. This suggests that the texture metrics were more sensitive to rubbly pāhoehoe, as this was included in the Rough class as opposed to the smoother Pāhoehoe class in the Definition-based classification. This change in class may have been responsible for the lower differences. This reinforces the use of GLCM to capture true physical roughness differences between morphologies, which could be used to automate the labeling of clustered segments through an average value comparison (i.e. by comparing cluster 1 values to cluster 2 values and assigning labels based on which pattern the values follow), or potentially used alongside the Sentinel-1 and Sentinel-2 data to enhance classification accuracy, especially with regards to classifying transitional lava flows as their own categories by thresholding GLCM values in each group. A statistical comparison of the four metrics used here, and potentially other GLCM metrics, would be the logical next step in evaluating their significance, but this was outside the scope of the present study, as the GLCM analysis was intended as an exploratory component.

5.2 Terrain Influences on Classification Accuracy

The Mann-Whitney U test and Cliff's Delta revealed that certain terrain variables had influence on classification results. The Sentinel-2 (C0_P6) data was the most influenced by terrain aspect, with Northness having a high significance (p-value of 2.45e-06, effect size medium). This aligns with the well-established issue where sloping terrain distorts optical reflectance values due to illumination and shadow effects, which can lead to lower landcover classification accuracy, especially in mountainous areas (Chen et al., 2023). The Sentinel-2 L2A product used underwent terrain correction, greatly improving reflectance uniformity on slopes, however it does not perfectly correct for small scale local relief which can result in residual artifacts. This means residual errors include terrain over-correction where some areas get too bright, a documented issue in Sentinel-2 L2A data (Optical Mission Performance Centre, 2024) or under-correction, where some areas remain too dark due to self-shadowing. Self-shadowing is caused by small surface roughness/texture or fine-scale relief (microtopography features). This distorts spectral signals by reducing the amount of reflected light reaching the sensor in certain viewing angles/illuminations, which can lead to classification errors which are more pronounced for rougher surfaces (Alavipanah et al., 2022). These errors are caused by Copernicus's global 90 m DSM used when the L2A product is generated (Optical Mission Performance Centre, 2024), as the DSM fails to correct for microtopography at scales smaller than its resolution (Wu et al., 2019). In addition to this, the Copernicus GLO-90 DSM was created using TanDEM-X data from between 2011 and 2015 (Optical Mission Performance Centre, 2024), meaning this terrain correction is not optimal in volcanically active areas. These errors have been observed in other land cover classification studies, where shading caused misclassification issues by reducing reflectance which led to some shaded surfaces being mistaken for different land cover types (Tayer et al., 2023). Overall, the effect of terrain suggests that optical classification of lava flows is sensitive to terrain aspect, specifically north-facing slopes. This aligns with the direction of Sentinel-2's orbit and the sun's southerly position for locations in the northern hemisphere at the time the image is captured. North-facing slopes receive less illumination causing shadowing and potentially over-correction in some places, or under-correction due to increased self-shadowing on rubbly pāhoehoe, leading to more misclassifications.

For the Sentinel-1 (C2_P5) data, no terrain variable had a significant effect on the results. SAR sensors are not sensitive to solar illumination due to being active sensors and also benefit from radiometric terrain correction which further removes residual topographic effects (Flores-Anderson et al., 2023). These results can explain why the Multi-Sensor (C13_P5) data was less influenced by terrain aspect. The Cliff's Delta effect sizes for Northness and Eastness are lower for C13_P5 (multi-sensor) when compared to C0_P6 (Sentinel-2). The effect size of Northness went from being medium to small, and for Eastness from small to negligible. This indicates that the addition of Sentinel-1 data slightly lowered the influence of terrain effects on the classification, which could be responsible for the slight increase in OA (0.25 percentage point difference) between using only Sentinel-2 data vs. combining it with Sentinel-1 data for Definition-based classification.

5.3 Implications for Lava Flow Mapping

The results of this study have implications for improving lava flow mapping and hazard monitoring in high-eruption-frequency areas like at Mount Kīlauea. The ability to accurately classify lava flow morphologies using freely available remote sensing data can enhance the understanding and practical response to volcanic events. Here, I will discuss the key applications and considerations coming from this study's findings, including near-real-time hazard monitoring, field survey prioritization, and usage in inaccessible or high-risk environments.

5.3.1 Near-Real-Time Hazard Monitoring

Being able to identify pāhoehoe and ʻa'ā lava flow morphologies during on-going eruptions, even when optical conditions may not be favourable, has the potential to aid emergency management agencies. When exposed to the air, an active lava flow will form a strong, solid crust on its surface within minutes (Kilburn, 2000), making this ideal for near-real-time classification.

Figure 9. Left: ʻAʻā lava flow originating from Fissure 8 on Kīlauea's lower East Rift Zone on June 1, 2018, showing how the surface of the flow cools and solidifies as it continues to advance (USGS photo courtesy of A. Lerner, as reproduced in West Hawaii Today, 2019). Right: Pāhoehoe channel coming from the Fissure 8 cone on June 24, 2018, showing that the surface of the flow begins to solidify within moments of breaching the surface (U.S. Geological Survey, public domain).

Knowing the morphology of the lava flow can provide information on hazard potential due to the nature of the flow mechanics involved in creating these morphologies. For example, ʻa'ā flows typically advance as massive, fast-moving rubble piles with high flow fronts, generally moving faster than pāhoehoe at speeds reaching up to 10 km/h down steep slopes (Lockwood et al., 2022, p. 153), potentially threatening infrastructure found along the flow's path. Smooth pāhoehoe flows tend to flow slowly, often in a stop-and-go fashion, where individual lobes form, cool, and inflate sequentially, with common speeds as low as 1 m/min, though speeds as fast as 30 km/h have been observed within confined channels and conduits within the interior of the flow well upslope (Lockwood et al., 2022, p.153). Therefore, near-real-time critical hazard information can be extracted by fully exploiting complementary sensors, something Corradino et al. (2021) highlighted the need for. This could ultimately contribute to better-informed decisions, like evacuations or road closures, as authorities have a detailed picture of the ongoing eruption's products.

5.3.2 Field Survey Prioritization

Creating detailed classification maps of lava flow morphologies can assist volcanologists when planning fieldwork and post-eruption surveys. Because conducting fieldwork around fresh lava flows is challenging, risky (especially in high-eruption-frequency areas), and often resource-intensive, having prior classification maps allows researchers to prioritize which areas to visit, and what observations to focus on. For example, the map created in this study of the 2018 lower ERZ flow could be studied to identify certain pāhoehoe lobes amongst predominantly 'a'ā flows (or vice-versa), which may represent transitional areas or changes in eruption conditions. By targeting such areas volcanologists/geologists in the field can i) validate the classification and ii) collect samples or measurements that explain why the flow morphology changed in these specific areas. Another example of how knowing the general morphology of the lava flow ahead of time can be useful in fieldwork planning is the "Survival Tip for Field Volcanologists" provided by Lockwood et al. (p. 155, 2022), stating that the outer margins of young 'a'ā flows are commonly hazardous places to climb due to the clinkery rubble being loose and unconnected to interior parts of the flow. This means that attempts to climb could result in the flow crumbling under the person's weight. As such, the middle and near-vent sides of these flows are safer to climb as they are thinner, and the fragments tend to be fused to each other or the interior parts of the flow (Lockwood, p. 155, 2022).

Based on a classified map, researchers can navigate to key locations with GPS, rather than conducting extensive reconnaissance, which is time consuming and expensive. This efficiency not only saves time and cost but also improves safety as field crews spend less time exposed to heat, unstable surfaces, and noxious gases. Additionally, the map could also inform what equipment or strategies to use. For example, if an area is mapped as extensive 'a'ā, it will be much more difficult to traverse than pāhoehoe, meaning that deploying a drone might be prioritized over sending a researcher on foot. Pāhoehoe on the other hand would be more easily traversable, allowing for researchers to walk larger distances to make observations up close.

5.3.3 Use in Inaccessible or High-Risk Environments

Remote sensing classification approaches are particularly interesting for volcanoes that are difficult or dangerous to access. Many active volcanoes around the world are in remote locations or have conditions that prevent them from being observed up close (for example, eruptions in war-torn countries, flows on steep and unstable terrain, or remote emerging volcanic islands). In such locations, satellite-derived morphology maps may be the only feasible way to get information on the lava flows. By leveraging satellites that provide frequent, free, and global coverage, a volcano may be monitored regardless of location. This is especially relevant for high-eruption-frequency volcanoes where the terrain can change quickly as new lava flows begin to overlap older flows. Additionally, having morphological classification in inaccessible areas allows for the inclusion of those eruptions in comparative studies that historically would have required fieldwork. Over time, this could contribute to our understanding of why certain eruptions produce more than one lava flow morphology and could improve modeling of flow emplacement.

The multi-sensor approach tested in this study offers some advantages in these remote locations as well. While optical imagery provides high sensitivity to surface reflectance differences between the morphologies, it is limited by cloud cover, ash plumes, and illumination geometry. SAR, in contrast, can penetrate clouds and works independently of sunlight. By integrating these data sources classification accuracy can be maintained across a wider range of conditions. An example of the multi-sensor approach being preferred over the use of only optical data is when shadowed slopes are prevalent. The multi-sensor approach may reduce omission errors by improving the classification of subtle textures, especially in this context.

5.4 Challenges and Limitations

5.4.1 Sensor Limitations

Though one of the goals of this study was to use freely available data, this did not come without its own set of limitations which have affected the overall accuracy of the classification results. The classification of lava flow morphologies using Sentinel-1 C-band SAR is still affected by speckle noise, despite the application of a Refined Lee Speckle filter. The window size used by this function is meant to balance speckle suppression and detail preservation, allowing for the effective reduction of noise while maintaining important surface features and edges necessary for accurate texture analysis (Kupidura, 2016). Despite this, some SAR band combinations had to be excluded early in the analysis as the results produced overly simplified segments, removing the clarity of the lava flow boundaries. This is a known challenge when using SAR data for geological classifications (Gaddis et al., 1990; Xie et al., 2021).

Due to the C-band wavelength (5.6 cm) being most sensitive to surface roughness at the centimeter to decimeter scale, rubbly pāhoehoe and ‘a‘ā were harder to differentiate in the Definition-based classification, as both exhibit similar roughness at the decimeter to meter scale (Tolometti et al., 2020). Previous studies have shown that C-band SAR struggles to distinguish surfaces with comparable roughness characteristics, leading to similar backscatter values, particularly in transitional lava flow areas (Tolometti et al., 2020; Dabiri et al., 2021). This limitation likely reduced the overall accuracy of the lava flow differentiation in the Definition-based classification.

The final limitation was the spatial resolution of the imagery used. While a 10-m resolution is considered high in some contexts, it contributes to the mixed pixel issue inherent with remote sensing. This issue can lead to the misclassification of lava flows, particularly in areas where the two classes mix at a smaller scale, creating confusion when the band combination mean values around the edges of the segments include both lava types (Aufaristama et al., 2019; Byrnes et al., 2004). This applies to the validation polygons as well, since they were derived from very high-resolution drone imagery, which allowed for more precise delineation of lava flows at fine scales, particularly in areas where overlapping textures occurred within a single 10 m^2 pixel.

5.4.2 Validation Data Limitations

Due to limitations with the drone model used, the flights were done manually without the help of a flight planner. For this reason, the images did not overlap sufficiently to create an accurately georeferenced orthomosaic on its own, thus needing to find an outside dataset for Ground Control Points (GCPs). This issue was mitigated by using the LiDAR-derived DEM also used to create the slope and aspect layers (Mosbrucker et al., 2020); this DEM was used to create the GCPs, which in turn were used to georeference the drone imagery.

Another limitation of the drone was its battery life, which meant it could only be safely flown to and from the liftoff location for ~10 minutes per battery. This meant that large distances could not be covered during the flights, with the longest of the nine flights having covered a total distance of about 1 km. The thickness of the lava flow in certain flight locations also limited the range at which the drone could be flown, as visual contact had to be kept with the drone to comply with local drone flying regulations. In some areas, such as where flights 1, 2, 5, and 6 were located, the lava at the edge was ~ 3 – 5 m thick, hindering line of sight considerably. Additionally, there were limitations due to road accessibility. The lava flow covered such a large area that it flowed over many roads that had not been rebuilt at the time of field work. Additionally, many areas were inaccessible due to being private property roads. Only a few public locations around the edges of the flow, and the areas where roads have been rebuilt, were accessible. A resulting limitation of this study is therefore the quantity and distribution of the drone imagery.

Despite these limitations, the results are still valuable for assessing the performance of the classification models, the value of incorporating Sentinel-1 and Sentinel-2 data for lava flow mapping, and for identifying factors that influence the classification accuracy.

5.5 Potential for Future Work

One of the main implications of this study is the potential for automating lava flow morphology mapping in the future. The results show that object-based segmentation combined with clustering and GLCM texture analysis can achieve high accuracies without the need for manual digitization. The clear differences in GLCM texture metrics between ‘a’ā and pāhoehoe, especially Contrast and Entropy, provide quantitative data that could be translated into automated decision rules based on GLCM thresholds for each class. The GLCM texture features used in this study therefore present an opportunity to not only automatically label the clustered segments but may also be useful in classifying lava flow morphologies, including subclasses such as rubbly pāhoehoe and clinker ‘a’ā. In order to do this, however, more data would have to be collected over a variety of lava flow morphologies in different locations to allow for robust definitions of GLCM-based thresholds. Evaluating other GLCM texture metrics would also be beneficial, such as correlation, autocorrelation, cluster prominence, and cluster shade, among others which were not used in this study. This may also provide information that can be used to threshold lava flow morphology classes/subclasses.

While the research focused on two generalized lava flow morphology categories, pāhoehoe and ‘a’ā, future work could broaden these classification categories to provide a more nuanced representation of possible lava flow morphologies. This would involve including subcategories such as rubbly pāhoehoe, ‘a’ā clinker, blocky lava (if applied to non-basaltic flows), and/or other transitional morphologies, as their own classes. This could offer deeper insights into the complexities of lava flow surface characteristics based on smaller-scale textural differences. One example of an area that would have benefited from a ‘rubbly pāhoehoe’ category in this study is the area where flight 2 was done (Figure 6). Much of the area covered in this flight consisted of rubbly pāhoehoe, as per both the field observations made in February 2024 and the drone imagery.

Another direction for future research could involve the investigation of the relationship between Sentinel-1’s incidence angle and local slope, which may have influenced the lower accuracy for the SAR-only classifications. Although radiometric terrain correction minimizes large-scale topographic effects, residual sensitivity to look angle remains. Small-scale facets such as clinker ridges, pāhoehoe slabs, and spiny textures can redirect SAR returns depending on their orientation, potentially inverting the expected backscatter values for the roughness type observed. One potential avenue for research into this could include grouping pixels into incidence-angle bins to evaluate how the viewing angle affects backscatter and classification performance. Such an analysis could improve understanding of geometric distortions on a complex lava surface.

Additionally, expanding the multi-sensor approach to include a wider range of SAR wavelengths could provide new insights into the lava flow morphologies. For example, data from the recently launched joint NASA-ISRO NISAR mission, could potentially enhance the detection of morphological differences at a larger scale due to the satellite having a dual-frequency system which operates in both L-band (24 cm wavelength) and S-band (9 cm wavelength) with a resolution of 3-10 m depending on the mode used (NASA, 2022). Commercial satellites such as ICEYE and Capella both offer X-band (3.1 cm wavelength) at much higher spatial resolutions, sub-3 m pixels, again depending on the mode. This could provide new capabilities for classifying the surface roughness of lava flows at higher resolutions and at a wider range of roughness scales. There are studies that show some limitations using L-band for morphology classification (Tolometti et al., 2020), however, it could still be beneficial for capturing the larger structure of blocky ‘a’ā. If combined with X-band and C-band, and/or optical imagery, this could potentially resolve some of the issues concerning spectral and backscatter similarities between transitional classes (Rogic et al., 2020). A combined, multi-frequency SAR methodology stacking X-, C-, and L-band imagery would likely enhance sensitivity to different roughness patterns and provide a more comprehensive understanding of lava flow morphologies. NISAR’s data is planned to be freely available and should be easy to integrate into a workflow such as the one used in this study, however X-band remains paid commercial data.

SAR Polarimetry is another direction that could add value. Fully polarimetric or quad-pol data can help separate different scattering behaviours, which might highlight textural differences that the VV and VH bands did not capture. For example, Polarimetric Decomposition could be done to break down the backscatter into different scattering mechanisms, such as Pauli Decomposition which separates SAR data into HH-VV, HH+VV, and VH components. These components highlight surface, volume, and double-bounce scattering, which would provide more information about the scattering properties of the lava flow morphologies (López-Martínez & Pottier, 2021).

Different SAR imagery pre-processing could also be explored in order to determine which speckle filtering method is best for lava flow morphology classification at this scale. The Refined Lee Speckle filtering (Lee, 1980) is widely accepted as a method for reducing noise in SAR imagery, however, it could also be worth considering speckle filters such as Gamma-MAP or Frost filtering, as these methods offer better edge and detail preservations (Kupidura, 2016), which may prove useful in lava flow morphology classification.

Finally, this study exclusively explored an unsupervised classification method. It could also be worth attempting supervised classification approaches. Supervised classifications have been used for mapping lava flow extents with some of the best models having accuracies of 96.7 - 99.8% in Iceland (Corona et al., 2024), though not much work has been done on lava flow morphology classification using these methods.

Chapter 6. Conclusion

6.1 Summary of Key Findings

The object-based classification method developed in this study successfully demonstrated the use of the freely available Sentinel-1 (SAR) and Sentinel-2 (optical) sensors in the classification of the two most common basaltic lava flow morphologies, pāhoehoe and ‘a’ā. The methods produced contiguous and coherent lava flow segments on the 2018 lower East Rift Zone (ERZ) eruption of Mount Kīlauea that closely resemble the known flow morphology boundaries. Six Segment Mean

Shift (SMS) parameter sets and sixteen three-band composites (single-sensor and multi-sensor) were tested, with the classification results validated using two methods: Definition-based (Pāhoehoe vs. ‘A‘ā) and Textural-based (Smooth vs. Rough). Overall classification accuracies were high, with the highest Definition-based classification yielding 86.31% overall accuracy (multi-sensor band combination C13 with SMS parameter set P4 or P5), and the Textural-based classification achieving 88.69% (single-sensor C0 with P6). This confirms that spectral and spatial signatures can be used to differentiate lava flow morphologies. The slight increase in accuracy between classification methods shows there is reduced confusion in the segmentation algorithm caused by the transitional rubbly pāhoehoe when it is included in the Rough class, as opposed to the Pāhoehoe class. Class-based metrics showed a systematic bias where Rough/‘A’ā had higher Producer Accuracies (~92-94%) than Smooth/Pāhoehoe (~75-78%). This indicates that smoother classes are more prone to omission errors. Part of this difference reflects true textural differences between the classes, but it is also influenced by class imbalance, where there is more than twice the amount of ‘A’ā/Rough as Pāhoehoe/Smooth in the 2018 lower ERZ flow. The validation data was representative of the whole lava flow, where the class imbalance reflects geological reality rather than methodological bias, though it makes the Producer Accuracy of the smaller Smooth/Pāhoehoe class more sensitive to misclassifications.

GLCM texture feature analysis confirmed consistent differences between classes, supporting the assumption that rougher surfaces would have higher contrast and entropy as well as lower homogeneity and energy. This supports the use of these texture features to further automate lava flow morphology classification and appear to be more sensitive to transitional lava flow morphologies.

Finally, terrain analysis showed that Sentinel-2 misclassifications were significantly ($p<0.05$) influenced by North-facing slopes, explained by the shadowing and self-shadowing effects due to the Sun's position at the time the image was captured. The multi-sensor band combination slightly lowered the terrain effect, while Sentinel-1 classifications were unaffected, with negligible terrain influence.

6.2 Contributions

This research aids in advancing the application of object-based classification for lava flow morphology mapping in multiple ways: SAR was found to be reasonably accurate (~77% OA) to map pāhoehoe and ʻaʼā lava flows in the event optical imagery is not available or has some cloud cover during time-sensitive live eruptions. However, under optimal conditions, a clear high-quality optical image can achieve better results for flow morphology differentiation. The findings also indicate that the multi-sensor approach could be utilized in the event that terrain variables, such as Northness, greatly impact the optical imagery, as SAR imagery did not appear to be affected by these variables. Having these options available will help in near-real-time monitoring of live eruptions, the planning of fieldwork with regards to safety and logistics, as well as for the mapping of remote or difficult-to-access volcanoes around the Earth.

By comparing the Definition-based and Textural-based validation methods, this study quantified how class definitions affect classification performance. By grouping the transitional rubbly pāhoehoe with the Rough class, overall accuracy was higher, but GLCM texture features were slightly less separable than when it was grouped with the Pāhoehoe class. Segment-level texture measures showed that rougher and smoother morphologies can be consistently differentiated. This is especially true with regards to the degree of separation between the GLCM values in the Definition-based classification. GLCM could potentially be used to further enhance the classification of transitional lava flows, as well as for the semi- or fully unsupervised classification, reducing the need for manual labeling, especially in cases where fieldwork cannot be conducted.

Finally, the assessment of terrain influences on classification results identified terrain-illumination interactions as a source of misclassification, particularly in the Sentinel-2 imagery. It was found that a multi-sensor approach can reduce the effects of slope aspect in specific use cases. Together, these contributions provide a tested, reproducible methodology for mapping common basaltic lava flow morphologies using freely available data.

6.3 Final Thoughts and Future Directions

Future research could build on this work in many ways. For example, future work could further refine and automate lava flow morphology mapping by expanding on the GLCM texture metrics used here. Transitional morphologies such as rubbly pāhoehoe, clinker ʻaʻā, and blocky lava could be distinct subclasses that GLCM-derived thresholds would help differentiate. Evaluating the differentiability of transitional morphologies would allow for classification maps to be more nuanced and give more detailed insights into the mechanics involved in creating these lava flow morphologies. In addition, testing additional GLCM metrics to enhance class separability could be beneficial, especially when evaluating transitional morphologies as their own classes.

C-band SAR was found to be useful in lava flow classification in some situations, however testing alternative SAR frequencies such as L-band from the NISAR mission and X-band from commercial sensors, could provide additional information that may prove useful in capturing roughness/texture differences at shorter and longer wavelengths. In addition to SAR, the comparison of the free optical imagery from Sentinel-2 and higher-resolution commercial imagery could offer insights into the potential benefits of an increased spatial resolution. Finally, rather than the unsupervised object-based approach used here, applying a similar exploratory workflow to a supervised machine learning approach, such as a Random Forest model or a Convolutional Neural Network (CNN) trained on field-validated data, could provide meaningful insights and gains in classification accuracy that could be worth exploring.

In conclusion, the research presented here demonstrated that object-based, multi-sensor and single-sensor classification of the lava flow morphologies pāhoehoe and ʻaʼā can achieve high accuracies under the conditions tested. By combining textural, spectral, and terrain information, this research provides a useful foundation for developing automated lava flow morphology mapping approaches in rapidly changing high-eruption-frequency or remote or difficult-to-access environments.

Appendix 1

Table containing all the Overall Accuracies of the classification results based on the 8 retained band combinations, 6 parameter sets for the Segment Mean Shift model, and both validation methods (Definition-based and Textural-based).

Band Combination ID	Parameter Set ID	Definition OA (%)	Textural OA (%)
C0	**P1**	**84.25**	**86.43**
C2	**P1**	**75.64**	**75.83**
C3	**P1**	**74.10**	**73.51**
C8	**P1**	**81.89**	**84.27**
C10	**P1**	**72.39**	**74.92**
C13	**P1**	**84.86**	**86.74**
C14	**P1**	**78.43**	**80.31**
C15	**P1**	**81.79**	**84.54**
C0	P2	84.54	86.91
C2	P2	75.01	75.50
C3	P2	76.20	76.12
C8	P2	82.37	84.00
C10	P2	71.41	74.12
C13	P2	85.36	87.36
C14	P2	80.51	81.88
C15	P2	80.18	83.44
C0	**P3**	**84.96**	**87.81**
C2	**P3**	**75.87**	**76.21**
C3	**P3**	**76.71**	**76.84**
C8	**P3**	**81.32**	**82.75**
C10	**P3**	**70.67**	**73.41**
C13	**P3**	**86.06**	**87.73**
C14	**P3**	**78.11**	**80.80**
C15	**P3**	**80.96**	**83.32**
C0	P4	85.68	88.16
C2	P4	69.99	68.87
C3	P4	74.25	74.01
C8	P4	36.72	39.90
C10	P4	72.67	75.47
C13	P4	86.31	87.80
C14	P4	78.70	81.10
C15	P4	79.20	82.37
C0	**P5**	**84.36**	**86.87**
C2	**P5**	**76.91**	**76.74**
C3	**P5**	**75.65**	**74.97**
C8	**P5**	**36.21**	**38.94**
C10	**P5**	**61.95**	**63.62**
C13	**P5**	**86.31**	**86.86**

C14	**P5**	**77.36**	**79.92**
C15	**P5**	**79.75**	**82.77**
C0	P6	86.06	88.69
C2	P6	75.36	74.60
C3	P6	76.90	77.30
C8	P6	81.81	83.63
C10	P6	73.36	75.98
C13	P6	85.80	86.52
C14	P6	78.90	81.79
C15	P6	80.88	82.88

Appendix 2

Accuracy metrics calculated for the 2nd best-performing sensor group for Definition-based (C0_P6) and Textural-based (C13_P4) classification methods. Accuracy metrics include User Accuracy (UA), Producer Accuracy (PA), and F1 Score, all in percentages.

Accuracy Metric	**Definition-Based Classification**		**Textural-Based Classification**	
	‘A’ā	**Pāhoehoe**	**Rough**	**Smooth**
UA (%)	84.82	88.95	90.61	82.02
PA (%)	94.68	71.64	91.22	80.94
F1 Score (%)	89.48	79.36	90.91	81.48

Appendix 3

Number of pixels per class. Demonstrates the class imbalance, where there are more than twice the number of pixels in the ‘A’ā and Rough classes.

	Definition-Based Classification		**Textural-Based Classification**	
	‘A’ā	**Pāhoehoe**	**Rough**	**Smooth**
Pixels	1407	685	1461	631

Appendix 4

Original imagery names downloaded from Copernicus Browser in 32-bit.

Sentinel-1 – Ascending Orbit:

- 2020-02-15-00_00_2020-02-15-23_59_Sentinel-1_IW_VV+VH_VH_-_linear_gamma0
- 2020-02-15-00_00_2020-02-15-23_59_Sentinel-1_IW_VV+VH_VV_-_linear_gamma0

Sentinel-1 – Descending Orbit:

- 2020-02-12-00_00_2020-02-12-23_59_Sentinel-1_IW_VV+VH_VH_-_linear_gamma0
- 2020-02-12-00_00_2020-02-12-23_59_Sentinel-1_IW_VV+VH_VV_-_linear_gamma0

Sentinel-2:

- 2020-02-12-00_00_2020-02-12-23_59_Sentinel-2_L2A_B02_(Raw)
- 2020-02-12-00_00_2020-02-12-23_59_Sentinel-2_L2A_B03_(Raw)
- 2020-02-12-00_00_2020-02-12-23_59_Sentinel-2_L2A_B04_(Raw)
- 2020-02-12-00_00_2020-02-12-23_59_Sentinel-2_L2A_B08_(Raw)
- 2020-02-12-00_00_2020-02-12-23_59_Sentinel-2_L2A_True_color

Bibliography

Abrams, M., Abbott, E., &; Kahle, A. (1991). Combined use of visible, reflected infrared, and thermal infrared images for mapping Hawaiian lava flows. *Journal of Geophysical Research*, 96(B1), 475. https://doi.org/10.1029/90jb01392

Ager, T. P. (2023). The essentials of SAR: A conceptual view of synthetic aperture radar and its remarkable capabilities (1st ed.). Thomas P. Ager.

Al Shehri, A., & Gudmundsson, A. (2019). Unsupervised classification of lava flows in Harrat lunayyir using remote sensing and GIS. *Arabian Journal of Geosciences*, 12(16). https://doi.org/10.1007/s12517-019-4707-3

Alavipanah, S. K., Karimi Firozjaei, M., Sedighi, A., Fathololoumi, S., Zare Naghadehi, S., Saleh, S., Naghdizadegan, M., Gomeh, Z., Arsanjani, J. J., Makki, M., Qureshi, S., Weng, Q., Haase, D., Pradhan, B., Biswas, A., & M. Atkinson, P. (2022). The shadow effect on surface biophysical variables derived from remote sensing: A Review. *Land*, 11(11), 2025. https://doi.org/10.3390/land11112025

Albattah, W., & Khan, R. U. (2025). Impact of imbalanced features on large datasets. *Frontiers in Big Data*, 8, 1455442.

Aldeghi, A., Carn, S., Escobar-Wolf, R., & Groppelli, G. (2019). Volcano monitoring from space using high-cadence planet CubeSat images applied to Fuego volcano, Guatemala. *Remote Sensing*, *11*(18), 2151.

Amici, S., Piscini, A., Buongiorno, M. F., & Pieri, D. (2013). Geological Classification of Volcano Teide by hyperspectral and Multispectral Satellite Data. *International Journal of Remote Sensing*, *34*(9-10), 3356–3375. https://doi.org/10.1080/01431161.2012.716913

Amici, S., Piscini, A., & Neri, M. (2014). Reflectance spectra measurements of Mt. Etna: A comparison with multispectral/hyperspectral satellite. *Advances in Remote Sensing*, *03*(04), 235–245. https://doi.org/10.4236/ars.2014.34016

Aufaristama, M., Hoskuldsson, A., Ulfarsson, M., Jonsdottir, I., & Thordarson, T. (2019). The 2014–2015 Lava Flow Field at Holuhraun, Iceland: Using airborne hyperspectral remote sensing for discriminating the lava surface. *Remote Sensing*, 11(5), 476. https://doi.org/10.3390/rs11050476

Aufaristama, M., Höskuldsson, Á., Ulfarsson, M. O., Jónsdóttir, I., & Thordarson, T. (2020). Lava flow roughness on the 2014–2015 lava flow-field at Holuhraun, Iceland, derived from airborne LiDAR and photogrammetry. *Geosciences*, *10*(4), 125.

Babb, J. L., Kauahikaua, J. P., & Tilling, R. I. (2011). The Story of the Hawaiian Volcano Observatory: A Remarkable First 100 Years of Tracking Eruptions and Earthquakes. *US Department of the Interior*, US Geological Survey.

Balaguera, S. M. D., Hölbling, D., Dabiri, Z., & BM, G. (2023). Lava Flow Mapping Using Sentinel-1 SAR Data at the Fagradalsfjall Volcano, Iceland. *GI_Forum 2023*, 11, 102-110.

Byrnes, J. M., Ramsey, M. S., &; Crown, D. A. (2004). Surface Unit Characterization of the Mauna Ulu flow field, Kīlauea volcano, Hawai'i, using integrated field and remote sensing analyses. *Journal of Volcanology and Geothermal Research*, 135(1-2), 169–193. https://doi.org/10.1016/j.jvolgeores.2003.12.016

Campbell, B. A. (2012). High circular polarization ratios in radar scattering from geologic targets. *Journal of Geophysical Research: Planets*, *117*(E6). https://doi.org/10.1029/2012je004061

Campbell, B. A., & Shepard, M. K. (1996). Lava flow surface roughness and depolarized radar scattering *Journal of Geophysical Research: Planets*, *101*(E8), 18941-18951.

Carr, B. B., Lev, E., Sawi, T., Bennett, K. A., Edwards, C. S., Soule, S. A., ... & Marliyani, G. I. (2021). Mapping and classification of volcanic deposits using Multi-sensor unoccupied aerial systems. *Remote Sensing of Environment*, *264*, 112581.

Carter, L. M., Campbell, D. B., & Campbell, B. A. (2011). Geologic studies of planetary surfaces using radar polarimetric imaging. *Proceedings of the IEEE*, *99*(5), 770–782. https://doi.org/10.1109/jproc.2010.2099090

Chevrel, M. O., Pinkerton, H., & Harris, A. J. (2019). Measuring the viscosity of lava in the field: A review. *Earth-Science Reviews*, *196*, 102852.

Cigna, F., Tapete, D., & Lu, Z. (2020). Remote sensing of volcanic processes and risk. *Remote Sensing*, *12*(16), 2567.

Cando-Jácome, M., & Martínez-Graña, A. (2019). Determination of primary and secondary lahar flow paths of the Fuego Volcano (Guatemala) using morphometric parameters. *Remote Sensing*, 11(6), 727. https://doi.org/10.3390/rs11060727

Cohen, J. (1988). Statistical Power Analysis for the Behavioral Sciences (2nd ed.). Routledge. https://doi.org/10.4324/9780203771587

Corona, C. M., Pedersen, G. B. M., Sigurdsson, J., & Heude, M. (2024). Automated Mapping of Lava: Classification of the Lava Flow Field From the 2021 Fagradalsfjall Eruption. *IGARSS 2024 - 2024 IEEE International Geoscience and Remote Sensing Symposium*, 3821–3825. https://doi.org/10.1109/IGARSS53475.2024.10641606

Corradino, C., Ganci, G., Cappello, A., Bilotta, G., Hérault, A., & Del Negro, C. (2019). Mapping recent lava flows at Mount Etna using multispectral sentinel-2 images and Machine Learning Techniques. *Remote Sensing*, *11*(16), 1916. https://doi.org/10.3390/rs11161916

Corradino, C., Bilotta, G., Cappello, A., Fortuna, L., & Del Negro, C. (2021). Combining radar and optical satellite imagery with machine learning to map lava flows at Mount Etna and Fogo Island. *Energies*, *14*(1), 197.

Chen, R., Yin, G., Zhao, W., Yan, K., Wu, S., Hao, D., & Liu, G. (2023). Topographic correction of optical remote sensing images in mountainous areas: A systematic review. *IEEE Geoscience and Remote Sensing Magazine*, 11(4), 125–145. https://doi.org/10.1109/mgrs.2023.3311100

Crown, D. A., & Ramsey, M. S. (2017). Morphologic and thermophysical characteristics of lava flows southwest of Arsia Mons, Mars. *Journal of volcanology and geothermal research*, *342*, 13-28.

Das, S., Basnet, P., Seidel, D., Röll, A., Ehbrecht, M., & Hölscher, D. (2025). Tree Architecture and Structural Complexity in Mountain Forests of the Annapurna Region, Himalaya. *Ecology and evolution*, 15(4), e71341. https://doi.org/10.1002/ece3.71341

Del Negro, C., Fortuna, L., Herault, A., & Vicari, A. (2008). Simulations of the 2004 lava flow at Etna volcano using the magflow cellular automata model. *Bulletin of Volcanology*, *70*(7), 805-812.

Di Fiore, F., Vona, A., Kolzenburg, S., Mollo, S., & Romano, C. (2021). An extended rheological map of pāhoehoe—'A 'ā transition. *Journal of Geophysical Research: Solid Earth*, *126*(7), https://doi.org/10.1029/2021JB022035.

Dierking, W. (2002). Quantitative roughness characterization of geological surfaces and implications for radar signature analysis. *IEEE Transactions on Geoscience and Remote Sensing*, 37(5), 2397-2412.

European Space Agency. (n.d.). Sentinel-2 mission overview. *Copernicus Open Access Hub*. Retrieved January 4, 2025, from https://documentation.dataspace.copernicus.eu/Data/SentinelMissions/Sentinel2.html

ESRI. (n.d.). Segment mean shift (spatial analyst). Segment Mean Shift (Spatial Analyst)-ArcGIS Pro | Documentation. https://pro.arcgis.com/en/pro-app/3.4/tool-reference/spatial-analyst/segment-mean-shift.htm

Flores-Anderson, A. I., Parache, H. B., Martin-Arias, V., Jiménez, S. A., Herndon, K., Mehlich, S., Meyer, F. J., Agarwal, S., Ilyushchenko, S., Agarwal, M., Nicolau, A., Markert, A., Saah, D., & Cherrington, E. (2023). Evaluating sar radiometric terrain correction products: Analysis-ready data for users. *Remote Sensing*, 15(21), 5110. https://doi.org/10.3390/rs15215110

Francis, P., & Rothery, D. (2000). Remote sensing of active volcanoes. *Annual Review of Earth and Planetary Sciences*, 28, 81–106. https://doi.org/10.1146/annurev.earth.28.1.81

Francis, P., & Oppenheimer, C. (2003). Volcanoes (2nd ed.). *Oxford University Press*.

Gaddis, L. R., Mouginis-Mark, P. J., & Hayashi, J. N. (1990). Lava flow surface textures-SIR-B radar image texture, field observations, and terrain measurements. *Photogrammetric Engineering and Remote Sensing*, 56(ISSN: 0099-1112).

Garcia, M. O., Pietruszka, A. J., Norman, M. D., & Rhodes, J. M. (2021). Kīlauea's Pu ʻu ʻŌ ʻō Eruption (1983–2018): A synthesis of magmatic processes during a prolonged basaltic event. *Chemical Geology*, *581*, 120391.

Gawarecki, S. J., Lyon, R. J. P., & Nordberg, W. (1965). Infrared spectral returns and imagery of the earth from space and their application to geologic problems. scientific experiments for manned orbital flight *American Astronautical Society, Science and Technology Series*. 4, 13-133.

Ghuffar, S. (2018). DEM generation from multi satellite PlanetScope imagery. *Remote Sensing*, *10*(9), 1462.

Google. (2024, March 6). Sentinel-1 Guide. Retrieved March 31, 2024, from https://developers.google.com/earth-engine/guides/sentinel1#colab-python

Guilbaud, M., Self, S., Thordarson, T., & Blake, S. (2005). Morphology, surface structures, and emplacement of lavas produced by Laki, AD 1783-1784. *Special Papers - Geological Society of America*, 396, 81

Hall-Beyer, M. (2017). GLCM Texture: A Tutorial v 3.0. University of Calgary, 3.0.

Han, Y., Tang, J., Liao, J., & Ling, J. (2024). Surface roughness analysis of side-polished fiber based on the importance of texture features. *Applied Physics B*, 130(9). https://doi.org/10.1007/s00340-024-08289-8

Hawaiian Volcano Observatory. (1999, May 27). *Volcano watch - pāhoehoe and 'a'ā lava flows*. U.S. Geological Survey. Retrieved January 15, 2023, from https://www.usgs.gov/news/volcano-watch-pāhoehoe -and-’a’ā-lava-flows.

Iverson, R. M., Schilling, S. P., & Vallance, J. W. (1998). Objective delineation of lahar-inundation hazard zones. *Geological Society of America Bulletin*, *110*(8), 972-984.

Kahle, A. B., Gillespie, A. R., Abbott, E. A., Abrams, M. J., Walker, R. E., Hoover, G., & Lockwood, J. P. (1988). Relative dating of Hawaiian lava flows using multispectral thermal infrared images: A new tool for geologic mapping of young volcanic terranes. *Journal of Geophysical Research: Solid Earth*, *93*(B12), 15239-15251.

Kilburn, C. R. (2000). Lava flows and flow fields. *Encyclopedia of volcanoes*, 291-305.

Kupidura, P. (2016). Comparison of filters dedicated to speckle suppression in SAR images. *The International Archives of the Photogrammetry, Remote Sensing and Spatial Information Sciences*, *XLI-B7*, 269–276. https://doi.org/10.5194/isprsarchives-XLI-B7-269-2016

Lee, J. S. (1980). Digital image enhancement and noise filtering by use of local statistics. *IEEE Transactions on Pattern Analysis and Machine Intelligence*, 2(2), 165–168. https://doi.org/10.1109/TPAMI.1980.4766994

Lemenkova, P. (2021). Evaluating land cover types from Landsat TM using SAGA GIS for vegetation mapping based on ISODATA and K-means clustering. *Acta Agriculturae Serbica*, 26(52), 159–165. https://doi.org/10.5937/AASer2152159L

Li, L., Bakelants, L., Solana, C., Canters, F., & Kervyn, M. (2017-a). Dating lava flows of tropical volcanoes by means of spatial modeling of vegetation recovery. *Earth Surface Processes and Landforms*, *43*(4), 840-856.

Li, L., Solana, C., Canters, F., Kervyn, M. (2017-b). Testing random forest classification for identifying lava flows and mapping age groups on a single Landsat 8 image. *Journal of Volcanology and Geothermal Research*, 345, 109–124. https://doi.org/10.1016/j.jvolgeores.2017.07.014

Lockwood, J. P., Hazlett, R. W., & de la Cruz-Reyna, S. (2022). *Volcanoes: global perspectives*. John Wiley & Sons.

López-Martínez, C., & Pottier, E. (2021). Basic Principles of SAR Polarimetry. In *Polarimetric Synthetic Aperture Radar : Principles and Application* (Vol. 25, pp. 1–58). essay, Springer Nature.

Lu, Z., Rykhus, R., Masterlark, T., & Dean, K. G. (2004). Mapping recent lava flows at Westdahl Volcano, Alaska, using radar and optical satellite imagery. *Remote Sensing of Environment*, *91*(3-4), 345-353.

Macdonald, G. A. (1972). *Volcanoes* (1st ed.). Prentice-Hall.

Malaguti, A., Rosi, M., Di Muro, A., & Papale, P. (2024). Machine learning insights into the last 400 years of Etna lateral eruptions from historical volcanological data. *Geosciences*, 14(11), 295. https://doi.org/10.3390/geosciences14110295

Mann, H. B., & Whitney, D. R. (1947). On a test of whether one of two random variables is stochastically larger than the other. *The Annals of Mathematical Statistics*, 18(1), 50–60. https://doi.org/10.1214/aoms/1177730491

Maiti, P., Mandal, D., & Ghosh, P. (2021). A K-means clustering–based approach for 3D mapping and characterization of rock faces using digital images. *Arabian Journal of Geosciences*, 14(12), 2956. https://doi.org/10.1007/s12517-021-07209-w

Mastin, L. G., Christiansen, R. L., Swanson, D. A., Stauffer, P. H., & Hendley II, J. W. (1999). Explosive eruptions at Kīlauea volcano, Hawai'i? (No. 132-98). U.S. Geological Survey.

Mazzarini, F., Pareschi, M. T., Favalli, M., Isola, I., Tarquini, S., & Boschi, E. (2007). Lava flow identification and aging by means of lidar intensity: Mount Etna Case. *Journal of Geophysical Research*, *112*(B2). https://doi.org/10.1029/2005jb004166

Meissel, K., & Yao, E. S. (2024). Using Cliff's Delta as a non-parametric effect size measure: An accessible web app and R tutorial. *Practical Assessment, Research & Evaluation*, 29(2). https://doi.org/10.7275/pare.1977

Mohamed, A. S. S., & Lu, J. (2015). Analysis of GLCM Parameters for Textures Classification on UMD Database Images. *Proceedings of the Fifth International Conference on Advanced Communications and Computation (INFOCOMP 2015),* 111-116. IARIA.

Musacchio, M., Silvestri, M., Rabuffi, F., Buongiorno, M. F., & Falcone, S. (2021). Kīlauea–Leilani 2018 lava flow delineation using Sentinel 2 and Landsat 8 Images. *Geological Society, London, Special Publications*, *519*(1). https://doi.org/10.1144/sp519-2020-118

National Aeronautics and Space Administration. (2022, December 5). Quick facts. NISAR NASA-ISRO SAR Mission. https://nisar.jpl.nasa.gov/mission/quick-facts/

Neish, Catherine D., & Carter, L. M. (2014). Planetary radar. *Encyclopedia of the Solar System*, 1133–1159. https://doi.org/10.1016/b978-0-12-415845-0.00053-0

Neish, C. D., Hamilton, C. W., Hughes, S. S., Nawotniak, S. K., Garry, W. B., Skok, J. R., Elphic, R. C., Schaefer, E., Carter, L. M., Bandfield, J. L., Osinski, G. R., Lim, D., & Heldmann, J. L. (2016). Terrestrial analogues for lunar impact melt flows. *Icarus*, *281*, 73–89. https://doi.org/10.1016/j.icarus.2016.08.008

Oppenheimer, C. (1997). Surveillance and mapping of volcanoes and their emissions by satellite remote sensing. *Geography, 82*(4), 317–333.

Optical Mission Performance Centre, European Space Agency. (2024, April 10). *Sentinel-2 MSI Level-2A data quality report* (Issue 84.0; Ref. OMPC.CS.DQR.002.03-2025). Copernicus Sentinel-2 Mission.

Orynbaikyzy, A., Plank, S., Vetrita, Y., Martinis, S., Santoso, I., Dwi Ismanto, R., Chusnayah, F., Tjahjaningsih, A., Suwarsono, Genzano, N., Marchese, F., Rokhis Khomarudin, M., & Strunz, G. (2023). Joint use of sentinel-2 and sentinel-1 data for rapid mapping of volcanic eruption deposits in Southeast Asia. *International Journal of Applied Earth Observation and Geoinformation*, 116, 103166. https://doi.org/10.1016/j.jag.2022.103166

Oxford University Press. (n.d.-a). Aa, n.². In Oxford English dictionary. Retrieved August 17, 2025, from https://doi.org/10.1093/OED/3105643651

Oxford University Press. (n.d.-b). Pahoehoe, n. In Oxford English dictionary. Retrieved August 17, 2025, from https://doi.org/10.1093/OED/1052233400

Patrick, M. R., Dehn, J., Papp, K. R., Lu, Z., Dean, K., Moxey, L., Izbekov, P., & Guritz, R. (2003). The 1997 eruption of Okmok Volcano, Alaska: A synthesis of remotely sensed imagery. *Journal of Volcanology and Geothermal Research*, *127*(1-2), 87-105.

Papageorgiou, E., Foumelis, M., Trasatti, E., Ventura, G., Raucoules, D., & Mouratidis, A. (2019). Multi-sensor SAR geodetic imaging and modelling of Santorini volcano post-unrest response. *Remote Sensing*, *11*(3), 259.

Peckyno, R. (2010, June 5). What are the different types of basaltic lava flows and how do they form? *Volcano World*. Retrieved September 21, 2022, from https://volcano.oregonstate.edu/faq/what-are-different-types-basaltic-lava-flows-and-how-do-they-form.

Peterson, D. W., & Tilling, R. I. (1980). Transition of basaltic lava from pāhoehoe to ‘a’ā, Kīlauea Volcano, Hawaii: field observations and key factors. *Journal of Volcanology and Geothermal Research*, *7*(3-4), 271-293.

Philpotts, A. R., & Ague, J. J. (2009). Principles of igneous and metamorphic petrology. *Cambridge University Press*.

Purinton, B., & Bookhagen, B. (2020). Multiband (X, C, L) radar amplitude analysis for a mixed sand- and gravel-bed river in the eastern Central Andes. *Remote Sensing of Environment*, 246, Article 111799. https://doi.org/10.1016/j.rse.2020.111799

Pyle, D. M., Mather, T. A., & Biggs, J. (2013). Remote sensing of volcanoes and volcanic processes: integrating observation and modelling–introduction. *Geological Society, London, Special Publications*, *380*(1), 1-13.

Mosbrucker, A., Zoeller, M. H., & Ramsey, D. W. (2020). *Digital elevation model of Kīlauea Volcano, Hawaii, based on July 2019 airborne lidar surveys* [Data set]. USGS Volcano Science Center. https://doi.org/10.5066/P9F1ZU80

Myers, B., & Driedger, C. L. (2008). Eruptions in the Cascade Range during the past 4,000 years (No. 63). *US Geological Survey*.

Sehlke, A., Whittington, A., Robert, B., Harris, A., Gurioli, L., & Médard, E. (2014). Pahoehoe to aa transition of Hawaiian lavas: an experimental study. *Bulletin of Volcanology*, *76*, 1-20.

Sherrod, D. R., Sinton, J. M., Watkins, S. E., & Brunt, K. M. (2007). Geologic map of the State of Hawaii. *US geological survey open-file report*, *1089*(9), 1-85.

Sheth, H. (2003). The active lava flows of Kīlauea volcano, Hawaii. *Resonance*, *8*, 24-33.

Roberts, D. W. (1986). Ordination on the basis of fuzzy set theory. *Vegetatio*, 66(3), 123-131.

Rogic, N., Charbonnier, S. J., Garin, F., Dayhoff II, G. W., Gagliano, E., Rodgers, M., Connor, C. B., Varma, S., & Shean, D. (2023). Characterizing and Mapping Volcanic Flow Deposits on Mount St. Helens via Dual-Band SAR Imagery. *Remote Sensing*, 15(11), 2791.

Rösch, M., & Plank, S. (2022). Detailed Mapping of Lava and Ash Deposits at Indonesian Volcanoes by Means of VHR PlanetScope Change Detection. *Remote Sensing*, *14*(5), 1168.

Rouse, J. W., Haas, R. H., Schell, J. A., & Deering, D. W. (1973). Monitoring vegetation systems in the Great Plains with ERTS. *NASA Spec. Publ*, 351(1), 309.

Rowland, S. K., & Walker, G. P. (1990). Pāhoehoe and ‘a’ā in Hawaii: volumetric flow rate controls the lava structure. *Bulletin of Volcanology*, *52*, 615-628.

Rowland, S. K., Harris, A. J. L., Wooster, M. J., Amelung, F., Garbeil, H., Wilson, L., & Mouginis-Mark, P. J. (2003). Volumetric characteristics of lava flows from interferometric radar and multispectral satellite data: The 1995 Fernandina and 1998 Cerro Azul eruptions in the western Galápagos. *Bulletin of Volcanology, 65*, 311–330.

Tak, G. M., Park, J. H., Lee, C. K., & Kim, H. (2023). Influence of altitude, slope, and waterway characteristics on the occurrence of slow-moving landslides in South Korea. *Frontiers in Earth Science*, 11, 1276768. https://doi.org/10.3389/feart.2023.1276768

Tayer, T. C., Douglas, M. M., Cordeiro, M. C. R., Tayer, A. D. N., Callow, J. N., Beesley, L., & McFarlane, D. (2023). Improving the accuracy of the Water Detect algorithm using Sentinel-2, Planetscope and sharpened imagery: a case study in an intermittent river. *GIScience & Remote Sensing*, *60*(1). https://doi.org/10.1080/15481603.2023.2168676

U.S. Department of the Interior. (2021, June 7). 2018 eruption and summit collapse. National Parks Service. https://www.nps.gov/havo/learn/nature/2018-eruption.htm

U.S. Geological Survey - Hawaiian Volcano Observatory. (2018, September). Preliminary summary of Kīlauea Volcano's 2018 lower East Rift Zone eruption and summit collapse. Retrieved from https://www.usgs.gov/volcanoes/kilauea/kilauea-2018-summit-collapse-and-lower-east-rift-zone-eruption.

U.S. Geological Survey. (2018, June 24). Lava fountains from Fissure 8 entering lava channel, lower Puna [Photograph]. Public domain. U.S. Geological Survey. https://www.usgs.gov/observatories/hvo/news/volcano-watch-2018-eruption-kilauea-was-big-global-scale

West Hawaii Today. (2019, March 3). Volcano Watch: How do lava flows cool and how long does it take? Retrieved from https://www.westhawaiitoday.com/2019/03/03/hawaii-news/volcano-update/volcano-watch-how-do-lava-flows-cool-and-how-long-does-it-take

Whelley, P. L., Garry, W. B., Hamilton, C. W., & Bleacher, J. E. (2017). Lidar-derived surface roughness signatures of basaltic lava types at the muliwai a pele lava channel, Mauna Ulu, hawaiʻi. *Bulletin of Volcanology*, 79(11). https://doi.org/10.1007/s00445-017-1161-5

Wu, S., Wen, J., Gastellu-Etchegorry, J.-P., Liu, Q., You, D., Xiao, Q., Hao, D., Lin, X., & Yin, T. (2019). The definition of remotely sensed reflectance quantities suitable for rugged terrain. *Remote Sensing of Environment*, 225, 403–415. https://doi.org/10.1016/j.rse.2019.01.005

Xie, J., Li, Z., Zhou, C., Fang, Y., & Zhang, Q. (2018). Speckle filtering of GF-3 polarimetric SAR data with joint restriction principle. *Sensors, 18*(5), 1533. https://doi.org/10.3390/s18051533

Xu, H. (2006). Modification of normalised difference water index (NDWI) to enhance open water features in remotely sensed imagery. *International journal of remote sensing*, 27(14), 3025-3033.

Zhang, H., Wen, X., Xu, J., Luo, D., & He, P. (2020). Study on the Effect of Surface Roughness on the Spectral Unmixing of Mixed Pixels. *Journal of Spectroscopy*, 2020(1), 5796860.

Zhang, C., Soda, P., Bi, J., Fan, G., Almpanidis, G., García, S., & Ding, W. (2023). An empirical study on the joint impact of feature selection and data resampling on imbalance classification. *Applied Intelligence*, 53(5), 5449-5461.